SIMULATION AND EXPERIMENTAL INVESTIGATION OF BONE

"THROUGH-GROWTH" ON STABILITY OF INTERPOSITIONAL

ORTHOPEDIC IMPLANT

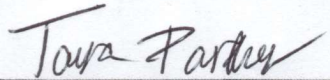AN ABSTRACT

SUBMITTED ON THE EIGHTH DAY OF MAY

TO THE DEPARTMENT OF BIOMEDICAL ENGINEERING OF THE

SCHOOL OF SCIENCE AND ENGINEERING OF TULANE UNIVERSITY

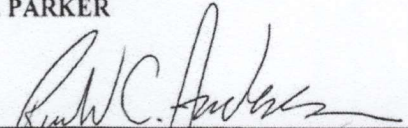IN PARTIAL FULFILLMENT OF THE REQUIREMENTS FOR THE

DEGREE OF

MASTER OF SCIENCE

BY:

_____

TARA A. PARKER

APPROVED: _____

Ronald C. Anderson, Ph.D., Advisor

_____

Uwe R. Pontius, M.D. Ph.D

_____

Khaled Adjerid, Ph.D

ABSTRACT

Knee osteoarthritis (OA) is one of the most common joint diseases in the world, affecting a staggering 86.7 million people worldwide in the year 2020. Osteoarthritis is characterized by the breakdown of cartilage in the joints, leading to pain, stiffness, and limited mobility in patients. Knee malalignment is an important predictor of knee OA. High tibial osteotomies (HTO) are an effective treatment for knee osteoarthritis particularly for patients with varus knee malalignment. The purpose of an HTO is to correct the load-bearing axis of the knee joint, redistributing the overload from the damaged medial compartment to the lateral compartment. While obesity is a common comorbidity to OA, it can be a contraindication for HTO's due to the increased load on the HTO plate. A newly patented HTO device has been developed to address this issue for obese patients. This device includes an implant that occupies the osteotomy space and provides additional mechanical strength. There are 5 openings or "windows" that go through this implant, to provide an opportunity for bone through-growth. This is a pilot study that focuses on how to optimize the windows' design to create better initial and long-term stability. Simulation and experimental testing procedures were developed. The radius of curvature on the edge of the windows and the amount of bone through-growth in the windows were varied. The maximum load for extraction was recorded and observations were made on the failure mechanisms of the implant-bone assembly. The results indicate that a sharper radius on the windows' edge increased the overall implant stability. It also found that greater through-growth depth resulted in superior stability within the assembly. The results provide a framework for future interpositional implant design and bone through-growth studies.

SIMULATION AND EXPERIMENTAL INVESTIGATION OF BONE

"THROUGH-GROWTH" ON STABILITY OF INTERPOSITIONAL

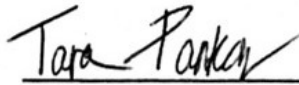## ORTHOPEDIC IMPLANT

A THESIS

SUBMITTED ON THE EIGHTH DAY OF MAY

TO THE DEPARTMENT OF BIOMEDICAL ENGINEERING OF THE

SCHOOL OF SCIENCE AND ENGINEERING OF TULANE UNIVERSITY

IN PARTIAL FULFILLMENT OF THE REQUIREMENTS FOR THE

DEGREE OF
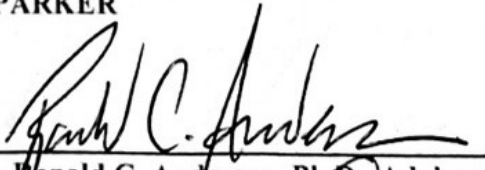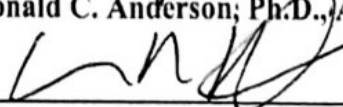
MASTER OF SCIENCE

BY:
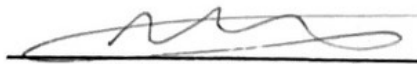
_____

TARA A. PARKER

APPROVED: _____

Ronald C. Anderson, Ph.D., Advisor

_____

Uwe R. Pontius, M.D. Ph.D

_____

Khaled Adjerid, Ph.D

ACKNOWLEDGEMENTS

TABLE OF CONTENTS

LIST OF TABLES

LIST OF IMAGES

CHAPTER 1: INTRODUCTION

Osteoarthritis (OA) is a common joint disease that is a leading cause of chronic disability (Heidari, 2011). It is characterized by the gradual breakdown of cartilage in the joints, leading to pain, stiffness, and limited mobility in patients (Heidari, 2011). Knee osteoarthritis is one of the most common types of osteoarthritis with an incidence of 86.7 million individuals worldwide in 2020 (Cui et al., 2020). The economic costs of knee OA are high and include treatment costs for affected individuals and their families as well as loss of income from individuals being unable to work (Heidari, 2011). Knee malalignment can act as a predictor for knee OA. Patients with knee malalignment are significantly more likely to develop knee OA as the forces acting on knee compartments are increased and concentrated in one compartment (Hunter et al., 2009). Patients with varus knee malalignment have 4 times the deterioration resulting from OA (Hunter et al., 2009).

The treatments for OA of the knee range from lifestyle changes and physical therapy to invasive surgical procedures. Surgical indication is based on the patient's age, level of physical activity, and comorbidities, in conjunction with radiological evidence and the level of the patient's suffering (Rönn et al., 2011). These factors direct the physicians to which of the treatments options are best suited for their patients. Two common surgical interventions for OA of the knee include Unicompartmental Knee Arthroplasty (UKA) and Total Knee Arthroplasty (TKA). A UKA is indicated for cases when only one of the compartments of the knee is badly affected (Rönn et al., 2011). A UKA is advantageous over a TKA because it is less invasive which means a shorter recovery time, preservation of bone, and usually better physiological function (Rönn et al., 2011). However, UKA has a significantly lower long-term survival than

TKA. The survival rate ranges from 80.2% to 98% at 10 years (Rönn et al., 2011). TKA is currently the most popular treatment option for advanced knee OA that affects more than one compartment of the knee, as it has a survival rate of 98% at 15 years (Rönn et al., 2011).

Obesity is a very common comorbidity to osteoarthritis. Obese patients are more likely to be diagnosed with OA at a younger age, develop more severe symptoms, and have a higher risk of infection from OA surgery (Chen et al., 2017). This is largely due to the increased weight acting on the knee joint that quickens the breakdown of cartilage. Obese patients have worse outcomes for UKA and TKA. Obese patients have a higher likelihood of revision surgery and have lower clinical outcome scores than non-obese patients after undergoing UKA (Campi et al., 2021). Morbidly obese patients that undergo TKA experience a higher rate of mid to long-term revisions. Even though they have similar functional recovery, they face a greater risk of surgical complications, including wound infection (Boyce et al., 2019).

High tibial osteotomies (HTO) are another surgical option for unicompartmental knee osteoarthritis patients with knee malalignment. HTOs differ greatly from UKAs and TKAs. The purpose of an HTO is to correct the load-bearing axis of the knee joint, unload the damaged compartment, and transfer the load from the affected areas while preserving the patient's bone stock (Khakha et al., 2021). An HTO is performed by creating an incision in the medial portion of the tibial to make an open wedge in the bone (Khakha et al., 2021). The wedge is held open by a metal plate and often filled with a graft material (Khakha et al., 2021). This procedure corrects knee malalignment and decreases the symptoms of knee osteoarthritis by moving the physical load from the damaged medial compartment to the lateral compartment (Khakha et al., 2021). This decreases the pain in the joint and prolongs the life of the knee joint (Khakha et al., 2021). Currently, obesity is a contraindication for HTOs because of the higher force on the medial plate

(Herbst et al., 2021). The procedure is still performed on obese patients; however, they have inferior clinical functional results compared to patients with lower BMIs (Herbst et al., 2021).

A newly patented design for an HTO implant seeks to solve these issues for obese patients. The MTOWI implant (Pontius, Patent WO 2020/014560 A1) is a multicomponent HTO implant for obese patients with medial compartment osteoarthritis and varus knee malalignment. The titanium alloy implant is intended to occupy the open wedge in the HTO procedure (Spillane et al., 2021). This design has been shown to supply the necessary mechanical support for the osteotomy in this high-loading environment while previous grafts or implants have proven insufficient.

Notably, the smaller components that make up this implant allow for a small surgical incision which should decrease the risk of infection in patients. This HTO implant design also considers the need for revision surgery and accommodates future TKA conversion. It does so by including a circular channel in the implant that aligns with the tibial intramedullary canal (Pontius, Patent WO 2020/014560 A1). This channel allows for insertion of a TKA tibial stem without HTO implant removal. There are four other openings or "windows" in the components of the implant (Pontius, Patent WO 2020/014560 A1). These are intended to allow the bone to grow within and add to component stability. However, what has not been tested is the effect of the design features of this window, specifically edge radius of curvature, and the stability of the implant during different periods post-operatively.

This preliminary study focuses on: how to potentially optimize the design of these windows to create the best placement and fixation, the amount of bone growth through the window, also known as bone "through-growth," and how edge stress concentration of the window geometry may affect the stability and potential migration of the inter-positional

orthopedic implant. The hypothesis is a sharper radius around the edge of a window will increase the necessary extraction force of a simple inter-positional implant, while the amount of through-growth will increase that extraction force for a given edge radius.

CHAPTER 2: BACKGROUND

2.1 Anatomy of the knee and tibia

The knee joint is the largest joint in the human body. It is the connection between the lower and upper leg. The knee joint is composed of bones, ligaments, cartilage, and synovium. The four bones that make up the knee joint are the femur, patella, tibia, and fibula (Gupton et al., 2022). The main ligaments that stabilize and provide strength to the joint are the anterior cruciate (ACL), posterior cruciate (PCL), medial collateral (MCL), and lateral collateral (LCL). The ACL inserts at the anteromedial aspect of the intercondylar area on the tibial plateau and originates at the posteromedial aspect of the lateral femoral condyle; it controls anterior translation of the tibia against the femur. The PCL originates at the anterolateral aspect of the medial femoral condyle and inserts along the posterior aspect of the tibial plateau. It prevents posterior translation of the tibia on the femur. The MCL originates on the medial aspect of the distal femur and inserts on the medial aspect of the proximal tibia. The function of the MCL is to accommodate valgus loading on the knee. The LCL originates at the lateral epicondyle of the femur and inserts distal to the fibular styloid tip. Its function is to accommodate varus loading on the knee (Gupton et al., 2022).

The knee is classified as a hinge joint, meaning it primarily allows for flexion and extension. It does also provide critical medial, lateral, as well as torsional functions. Therefore, it is considered a compound synovial joint (Gupton et al., 2022). The proximal face of the tibia and distal face of the femur are covered in articular cartilage. Synovial fluid lubricates and covers the cartilage on the bone surfaces. There are medial and lateral menisci which are located between the articular surfaces on the femur and tibia. These are fibrocartilaginous structures that reduce friction, absorb shock, and stabilize the joint. The knee has multiple bursas which reduce friction

between different structures. They are made of synovial membranes and contain synovial fluid (Gupton et al., 2022).

The knee joint has three main compartments: the patellofemoral compartment, and the medial and lateral tibiofemoral compartments. The patellofemoral compartment is the joint between the patella and the distal end of the femur, the femoral trochlea. The distal femur meets the proximal tibia at the tibiofemoral compartments. They comprise the main weight-bearing structures of the knee joint (Gupton et al., 2022).

Depending on a person's activity, the knee undergoes varying degrees of stress depending on the individual's body weight. The biomechanics of the knee is commonly considered in the context of two "phases" associated with the gait cycle: the stance phase and the swing phase (Bowker, 1992). The stance phase components consist of heel strike, foot flat, midstance, heel-off, and toe-off. The first phase of the gait cycle begins as the heel of an individual's foot touches the ground and ends as that same heel touches the ground again. As the heel touches the ground, the knee is extended between 0 and 5 degrees of flexion and torque is generated in the knee (Bowker, 1992). The quadriceps femoris is responsible for the knee extension. This results in 2.25 times body weight acting on the femoral head (Guo et al., 2009). After this, the moving foot is no longer touching the ground and the stationary foot bears the total body weight. This is termed "single stance" or "single leg stance." During this period, the stationary foot is stable. Knee flexion increases and reaches a maximum angle of 18 degrees when single stance begins. The motion then reverses to knee extension and the quadriceps femoris action is at a maximum. As the knee extends over the tibia, the flexor torque lessens and the quadriceps relaxes. 1.85 times body weight acts on the femoral head (Guo et al., 2009). The swing phase consists of toe-off, mid-swing, and heel-strike (Grujicic, 2022). Toe-off begins

when the stationary foot lifts off the ground. This requires 60 degrees of knee flexion and occurs from momentum in the leg that is supported by the biceps femoris, sartorius, and gracilis muscles. During toe-off, the femoral head experiences 3.5 times body weight (Guo et al., 2009). The multiplication of the forces on the knee results from the meniscus crossing the joint during activity, the angle between the hip-knee-ankle, and the muscles responsible for creating these motions.

Image 1 below gives the tibiofemoral contact force in multiples of body weight for a person engaged in 10 different activities according to a study by Sam van Rossom. This study was conducted on 15 healthy adults with the goal of understanding the specific forces acting on injury zones of patients to produce an exercise program for progressive knee loading (van Rossom, 2018). This graph demonstrates the wide range of loads that act on the knee during a person's activities. The contact forces for standing up and sitting down were relatively the same, averaging at less than 2 multiples of body weight. Whereas a single-leg hop push-off and single-leg hop weight acceptance averaged at 5 times a person's normal body weight (van Rossom, 2018). This, in accordance with the multiples of body weight from the gait cycle, demonstrates how much force can act on the knee during a person's regular activities. These multiples of body weight are important to consider when designing and comparing knee osteoarthritis treatments.
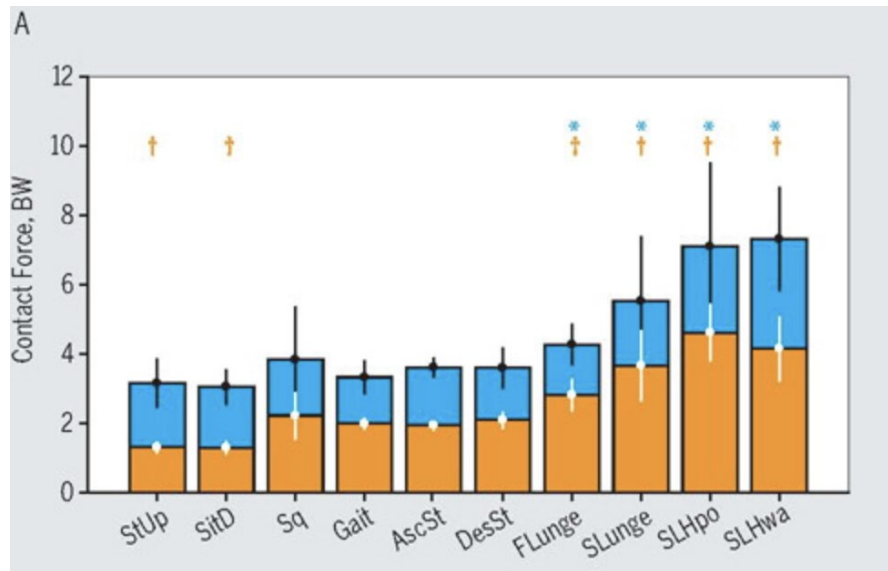
Image 1 Average (orange) and maximum (blue) tibiofemoral contact force during different exercises. Acronyms: StUp (stand-up), SitD (sit-down), Sq (squat), AscSt (ascending stairs), DesSt (descending stairs), FLunge (forward lunge), SLunge (sideward lunge), SLHpo (single-leg hop push off), SLHwa (single-leg hop weight acceptance) (van Rossom, 2018)

2.2 Osteoarthritis in the Knee:

Osteoarthritis (OA) is a degenerative joint disease. It is the most common joint disease and its incidence is increasing rapidly. The incidence of OA increases with age but can occur at any age due to excessive joint loading and joint injury. According to the Johnston County Osteoarthritis Project, 27.8% of participants over the age of 45 were diagnosed with OA of the knee (Zhang, 2010). There are numerous systemic and biomechanical factors that increase the risk of developing OA. Some systemic risk factors include age, sex, ethnicity, bone density, genetics, and nutritional factors. Biomechanical factors that can increase the risk of OA include obesity, joint injury, malalignment, physical activity, and muscle weakness. All these factors affect one's risk of developing OA and its severity. Obesity is an important risk factor for OA as the increased loading on the joint can lead to increased synovial joint deterioration.

There are currently no solutions to prevent or even slow the progression of OA. It is most common in the hands, knees, hips, neck, and back (Zhang, 2010). OA occurs when the tissue in

the joints begins to break down and deteriorate. Osteoarthritis in the knee can damage the cartilage, tendons, ligaments, synovium, meniscus, and bones of the knee as a result of localized inflammation. A knee joint experiencing OA undergoes loss of articular cartilage, degeneration of ligaments and menisci, thickening of the subchondral bone, formation of osteophytes, inflammation of the synovium, and hypertrophy of the joint capsule (Loeser, 2010).

Hyaline cartilage is the primary site of the harmful effects that cause osteoarthritis, and where the disease begins. Extracellular matrix (ECM) constitutes 95% of hyaline cartilage (Michael, 2010). Within the ECM, there is an ongoing dynamic equilibrium between the formation and breakdown of the cartilaginous matrix. The equilibrium is regulated by both anabolic and catabolic factors. These mechanisms can assist in improving the damage done by osteoarthritis by stimulating and modifying the metabolic activity of chondrocytes. When the damage exceeds the system's ability to compensate, matrix degradation occurs. This is said to happen because of mechanical and enzymatic factors that weaken chondrocyte function and therefore damage the matrix (Michael, 2010).

The cartilaginous breakdown that occurs from OA may result in contact between the femur and tibia. The contact causes pain, swelling, and stiffness in the joint. The breakdown of the cartilage may result in the formation of small, localized pockets within the joint space. These can fill with fluid and debris, which damages the surrounding tissues and causes pain and inflammation. As the disease progresses, small outgrowths of bone called osteophytes may develop around the joint which contributes to increased pain and discomfort (Michael, 2010). Sclerosis of the subchondral bone is also common. This refers to the hardening and thickening of the bone in response to stress from the OA (Lespasio, 2017). Osteoarthritis can also cause cleavage eburnation. Cleavage eburnation is the process of the bone becoming denser and more

polished due to increased friction and pressure within the joint (Ragier, 2006). This leads to the bone splitting and fracturing at the surface. The combination of these negative processes significantly impairs the function of the knee joint and causes significant pain to patients with OA.

OA causes numerous negative and painful symptoms in patients. The most common symptoms include pain while using the joint, joint stiffness, limited joint movement, swelling in and around the joint, and the feeling that the joint may be loose or unstable. OA can be a debilitating disease for the patients, especially when it comes to OA of the knee. Patients with OA of the knees often experience crepitation, which is a crackling and grating sensation in the joint (Pazzinatto, 2019). The physical effects can also lead to negative phsychological outcomes for the patients. Losing the ability to walk on one's own leads the patients to feel they are losing their bodily autonomy and freedom. They may even become clinically depressed (Wang, 2022).

Another important risk factor for OA is obesity. Obesity has become a worldwide epidemic and has many negative side effects for the patient's suffering from it. Over the past 30 years, worldwide obesity has more than doubled (King, 2013). Obesity is defined as having a BMI greater than 30 kg/m^2 by the National Institute of Health. The classifications for BMI and obesity can be seen below in **Table 1** (National Heart, Lung, and Blood Institute, 2000). Subjects with a BMI > 30 kg/m^2 are reportedly 6.8 times more likely to develop OA. BMI has a strong relationship with severe OA.

Table 1 Classifications for BMI according to NIH (National Heart, Lung, and Blood Institute, 2000)

Classifications for BMI	
	BMI
Underweight	<18.5 kg/m²
Normal weight	18.5–24.9 kg/m²
Overweight	25–29.9 kg/m²
Obesity (Class 1)	30–34.9 kg/m²
Obesity (Class 2)	35–39.9 kg/m²
Extreme obesity (Class 3)	≥40 kg/m²

People with obesity are more likely to be diagnosed with OA at a younger age. They are also more likely to develop more severe symptoms in association with OA. They have a higher risk of infection and are more prone to complications from surgeries (Chen, 2017). Obesity causes a greater mechanical load to be placed on the knees. For every 1 lb (0.45 kg) in weight gained, there is approximately 2 to 4 lbs (0.9 to 1.8 kg) of pressure on the knees (Lespasio, 2017). For every 5 unit increase in BMI, there is an associated 35% increased risk of knee OA (King, 2013). For example, a person who is 5 feet 10 inches tall is considered "normally weighted" at 170 lbs. If it is assumed that the knee experiences a force 3 times a person's body weight, then in the example above it could be anticipated that the knee is normally loaded to 510 lbs. If this person increases their normal weight by 50%, to 255 lbs, they have a BMI of 36.6 (National Heart, Lung, and Blood Institute, 2000) which is within the Obesity Class 2 range. The loading on the knee would now be expected to be 765 lbs, or 4.5 times their normal body weight. Knee loading at 4.5 times body weight is comparable to performing a lunge exercise with every stride of gait (van Rosson, 2018). At 285 lbs, BMI 41, the person is considered "morbidly obese," and would load their knee approximately 5 times body weight equivalent to performing a single-leg hop with each step (van Rosson, 2018).

The link between obesity and OA is caused by many factors. These include mechanical factors from increased loading, decreased muscle strength, altered biomechanical patterns, and

metabolic factors. One of the most important metabolic factors between obesity and OA is thought to be leptin, an adipokine. Leptin has receptors on the surface of chondrocytes, synoviocytes, and subchondral osteoblasts. It increases levels of degradative enzymes and produces pro-inflammatory cytokines. Chondrocytes from obese people exhibit a different response pattern to leptin than normal or overweight patients. Levels of leptin are significantly elevated in people with OA (King, 2013).

2.3 Knee Malalignment:

There are three main types of alignment for the hip, knee, and ankle: neutral, varus, and valgus knee alignment. This alignment determines how the load is distributed across the medial and lateral compartments of the knee. There is a mechanical axis that can be measured using a full-limb radiograph so one can assess the alignment of the knee (Schiraldi, 2016). **Image 2** shows the mechanical axis and anatomical axis in neutral alignment, as well as both axes in varus and valgus alignment. The mechanical axis starts at the center of the femoral head and passes through the knee joint to the center of the ankle (Liu et al., 2019). The axis from the femoral head to the intercondylar notch of the distal femur is called the femoral mechanical axis and the axis from the tibial proximal epiphysis to the center of the ankle joint is called the tibial mechanical axis. For neutral alignment, the femoral and tibial mechanical axis should make a medial angle that is slightly less than 180 degrees. This neutral alignment varies slightly by gender and genetics from person to person.
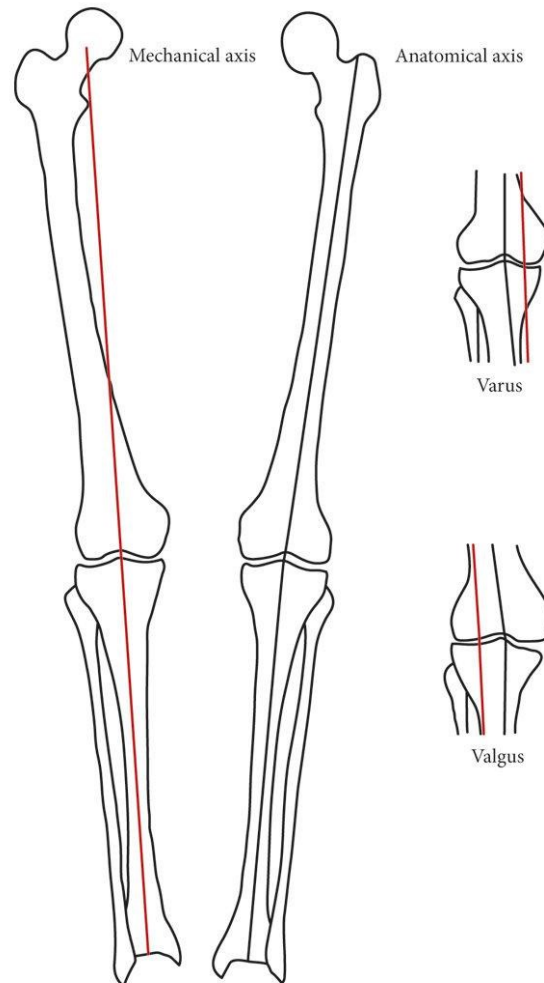
Image 2 Depiction of mechanical and anatomical axes at all three main types of alignment: neutral, varus, and valgus. The red line represents the mechanical axis, and the black line represents the anatomical axis (Liu et al., 2019)

For neutrally aligned limbs, 60-70% of the force from body weight is borne by the medial compartment during weight bearing. The medial compartment experiences further increased force with varus alignment. With valgus alignment, the force is increased on the lateral compartment and decreased on the medial compartment (Liu et al., 2019). These varying forces on the compartments of the knee are known to increase disease progression for OA in the knee. These increased forces lead to the destruction of the cartilage in those compartments. Varus malalignment predisposes the medial compartment to 4 times the progression of osteoarthritis; it

leads to bone marrow lesions and losses in cartilage. Cartilage loss results in more malalignment, creating a cycle that continuously increases the progression of osteoarthritis (Hunter et al., 2009).

2.4 Treatment Options:

Within the knee, arthritis can be present in specific areas or affect the entire joint. The study will focus primarily on medial compartment osteoarthritis for patients with varus knee malalignment. The arthritis is primarily focused in the medial compartment of the knee and the lateral compartment and patellofemoral joint are relatively unaffected (McCormack et al., 2021). There are non-surgical treatments for OA of the knee including oral pain medications, oral anti-inflammation medication, shock-absorbing footwear, and various supports to divide the load on the knee. There are also intra-articular injections of hyaluronic acid, steroids, and platelet-rich plasma (McCormack et al., 2021). These interventions can be helpful but are not effective in the long term.

The most common surgical intervention done for OA of the knee is a total knee arthroplasty (TKA), also known as a total knee replacement (TKR). In a TKR, the surgeon will remove all the damaged tissue in the knee on the tibia, femur and sometimes the patella. They will then replace this tissue with an articulating implant. TKA is the most frequently used surgical intervention for elderly patients with end-stage knee OA. However, considering that medial compartment OA only concerns one-third of the knee joint surface and leaves a significant amount of healthy tissue in the knee, there is no need to conduct this highly invasive procedure of replacing the whole knee joint (Wei et al., 2022).

TKA's should not be recommended for younger and more active patients with mild to moderate knee OA. In fact, around one-third of the TKRs for knee OA patients were said to have been "overtreatment" (Wei et al., 2022). This initiates use of the next two most common surgical

interventions which are unicompartmental knee replacement (UKR) and a high tibial osteotomy (HTO) (Wei et al., 2022). Both treatments are less invasive and have been attracting progressively more attention in recent years. A UKR is most like a TKA. Instead of replacing the entire knee joint, the surgeon only replaces the medial or lateral compartment of the joint where the tissue has deteriorated. This is a far less invasive procedure. Only the worn compartment is resected, and the rest of the knee is conserved. Recovery for a UKR is faster than for a TKA and the implant has a 10-year survival rate of 98% (Rönn et al., 2011).

An HTO procedure differs greatly from the TKA. Varus malalignment is the most frequently observed deformity in knee OA. It increases the load in the medial compartment, resulting in cartilage degeneration and arthritis (Khakha, 2021). The purpose of a HTO is to change the load-bearing axis of the knee joint and distribute a portion of the overload from the damaged medial compartment to the lateral compartment. There are numerous devices on the market used to perform an HTO. The most common HTO is performed by creating an incision in the tibia to make an open wedge in the bone. This wedge is held open by a metal plate. Locking screws are used to attach the plate to the bone superiorly and inferiorly to the wedge. Surgeons then use a variety of techniques to fill in this wedge or leave the open wedge unfilled. The material used to fill commonly takes the form of some type of graft, however synthetic void fillers such as calcium phosphate are sometimes used. Some studies have shown that allograft within the gap leads to increased integrity of the osteotomy (Khakha et al., 2021).

HTO corrects varus knee malalignment and decrease the symptoms of knee osteoarthritis. It decreases the pain in the joint, enhances the functionality of the knee, and prolongs the life of the knee joint. Due to the decrease of pressure in the medial compartment, there is an overall improvement in the health of the joint, reduced inflammation, and reduced pain. A new HTO

device has been patented by Dr. Uwe Pontius in 2020 that not only includes a plate but also includes an implant that fits within the wedge. The purpose of this implantable wedge is to support the weight placed on the limb (Spillane et al., 2021). Indications for an HTO include patients that are, moderately active, non-obese, having varus knee deformity, and a lack of joint instability (Khakha et al., 2021). Currently, HTOs for patients with a BMI>30 have been associated with poorer functional outcomes and increased adverse effects (Khakha et al., 2021). With the inclusion of the implantable wedge, HTOs become an option for obese and "high-impact" patients. This wedge implant can make HTOs a good option for obese patients who satisfy the indications mentioned above.

2.5 Description of Specific HTO Implant being studied

This study focuses on the newly patented Medial Tibial Open Wedge Implant (MTOWI), designed by Dr. Uwe Pontius and described in patent WO 2020/014560 A1. It is a multi-component implant for obese patients with medial compartment osteoarthritis and varus knee malalignment (Pontius, 2020). This titanium alloy implant is intended to occupy the open wedge in the high tibial osteotomy procedure (Spillane et al., 2021). Previous HTO procedures primarily used different types of graft material to encourage healing and occupy this space. The graft material does not provide early adequate mechanical support for osteotomies on obese patients. Ti-6Al-4V, on the other hand, has a compressive strength of 1070 MPa and provides the additional necessary support for obese patients to undergo HTO procedures (Sparr, 2022). The MTOWI implant consists of four interlocking components made of titanium alloy that will be assembled in situ. The interlocking components are referred to as "pluralities," and can be seen below in **Image 3 (a) and (b)**. The purpose of the pluralities is to minimize the surgical incision size which decreases the risk of surgical complications including infections (Spillane et al.,

2021). Each of these pluralities is 3D printed. The superior and inferior faces of the implant have a laser-sintered lattice structure that provides an environment for bone ingrowth. Bone ingrowth into the implant is necessary for the long-term success of the surgery. Ingrowth increases stability and the surface allows early full weight bearing after surgery. The ingrowth faces have a 550μm surface opening and 150μm internal pore size. The implant will be used in conjunction with a titanium alloy T-plate to provide initial stability (Spillane et al., 2021). One purpose of this implant is to correct varus knee deformity for medial compartment knee osteoarthritis in patients with a BMI of greater than 40.

High tibial osteotomies allow full activity and delay the need for a TKR surgery. The incidence of conversion from a medial opening wedge HTO to a TKR is 21% at 10 years (Khakha et al., 2021). This implant takes into account the need for conversion surgery and accommodates a future TKA by intentionally leaving space for necessary stem components in a TKA. TKA implants generally consist of a femoral component, spacer, and tibial component. The tibial component has a stem that inserts into the medullary canal of the tibia and provides mechanical stability and helps prevent loosening of the implant. The MTOWI Implant includes an opening that aligns with the medullary canal to allow the stem to enter the distal medullary canal.
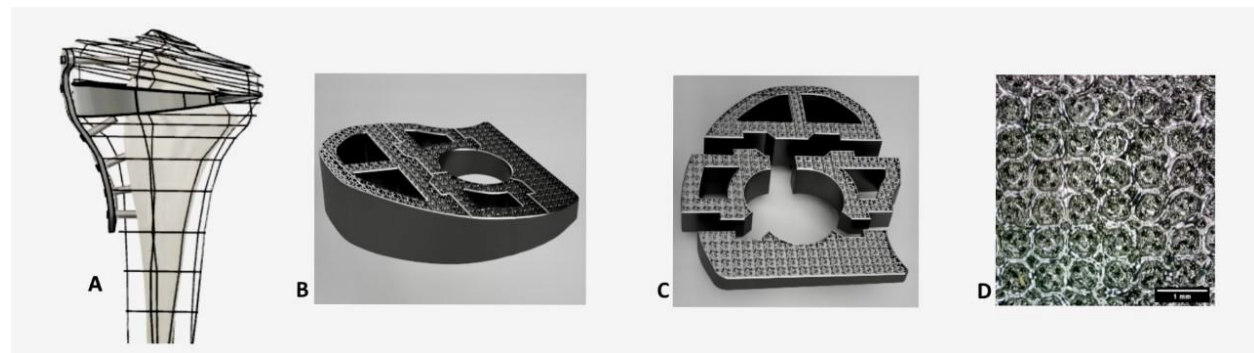
Image 3 (a): MTOWI Implant and Plate assembled in tibia using finite element modeling. (b): MTOWI implant pluralities assembled. (b): Pluralities non-assembled. (d): Laser-sintered 3-D lattice on the bone surface (Spillane et al., 2021)

This implant also incorporates 4 other openings or "windows" into the design. This study examines how windows in an orthopedic implant might affect implant stability within the bone. The study also varies the amount of bone "through-growth" through a window and the radius of the edge of a window to see how it affects mechanical stability.

2.6 Bone Healing/Fracture Healing:

The main cellular components of bone include the osteoprogenitor cells, osteoblasts, osteocytes, and osteoclasts. Osteoprogenitor cells, also known as osteogenic cells, are the stem cells of the bone. They are responsible for bone repair and growth and develop into osteoblasts and osteocytes. Osteoprogenitor cells are located in the periosteum and the bone marrow (Nahian & Davis, 2022). Osteoblasts are mature cells responsible for bone formation that can be found in the periosteum and endosteum. They secrete osteoid, which undergoes mineralization and strengthens the bone. Osteoblasts can transform into osteocytes or stay osteoblasts. Osteocytes are mature osteoblasts that remain in the bone matrix and maintain the mineral concentration of the matrix. Osteoclasts are developed from monocytes and macrophages and are responsible for bone reabsorption and remodeling (Betts et al., 2022).

There are two main types of bone: cortical and cancellous. Cortical bone, also known as compact bone, is dense and hard. Its basic unit is called an osteon which is made of concentric rings of a calcified matrix called lamellae. In the center of each lamella is a central canal containing blood vessels, nerves, and lymphatic vessels. This canal is called the Haversian canal. The vessels and nerves branch out from the canals through Volkmann canals that connect them to the endosteum and periosteum. Osteocytes are located between adjacent lamellae, in spaces called lacunae. Canaliculi connect the lacunae with each other and the central canals so waste can be removed, and nutrients can be delivered (Betts et al., 2022)

Cancellous bone, also referred to as spongy bone, shares similarities with cortical bone. Cancellous bone also contains osteocytes within lacunae, however, the arrangement of osteocytes and lacunae is different. Instead, they form a lattice-like network of matrix spikes called trabeculae. The trabeculae are formed along lines of stress to provide strength to the bone. The spaces of the trabeculae allow for bones to be lighter and less dense (Betts et al., 2022).

Bone healing is a complex regenerative process that involves many biological factors. It occurs in four main steps that are required to return the original mechanical and physical properties to the bone. These include the hematoma formation stage, the fibrocartilaginous formation stage, the bony callus formation stage, and the bone remodeling stage (Sheen & Garla, 2022). The hematoma formation stage takes place in the first 5 days after fracture. During fracture, the blood vessels and the periosteum is ruptured, and therefore a hematoma will form around the fracture site. This hematoma clots and forms a scaffold that assists for the duration of the fracture healing process. The fracture triggers the release of proinflammatory cytokines that facilitate cellular activity during healing. Macrophages, monocytes, and lymphocytes are attracted and help eliminate damaged, necrotic tissue and produce more cytokines to encourage healing (Sheen & Garla, 2022).

The fibrocartilaginous formation stage occurs during days 5-11 of the fracture healing process. Angiogenesis, the formation of new blood vessels, occurs in the hematoma when the vascular endothelial growth factor cytokine is released. Mesenchymal stem cells are attracted to the area and then differentiate into fibroblasts, chondroblasts, and osteoblasts. This leads to chondrogenesis, the process of cartilage production, and a fibrocartilaginous network forming at the ends of the fracture site. A layer of hyaline cartilage sleeve surrounds this. Osteoprogenitor cells also secrete a layer of woven bone by the periosteal layer (Sheen & Garla, 2022).

The bony callus formation stage occurs between days 11 and 28 after the fracture. Endochondral ossification starts at the fibrocartilaginous area. More differentiation of chondroblasts, chondroclasts, osteoblasts, and osteoclasts occurs. The cartilaginous callus that was created begins to get reabsorbed and calcifies. Woven bone is still being laid down under the periosteum. New blood vessels are still forming. The calcified callus of immature born has formed fully by the end of this phase (Sheen & Garla, 2022).

The bone remodeling phase starts at around day 18 post-fracture and can continue for weeks, months, or years afterward. The calcified callus undergoes repeated, "coupled remodeling." Coupled remodeling is a balance of new bone formation by osteoblasts and resorption by osteoclasts. There is also remodeling of vasculature occurring at the same time. This remodeling will last months and eventually results in the complete regeneration of normal bone structure (Sheen & Garla, 2022).

2.7 Bone Ingrowth vs. Bone Through-growth:

Bone ingrowth refers to the formation of bone within an irregular surface of an implantable device. The term bone ingrowth is often used with the term osseointegration, which refers to the contact between bone and the surface of an implant. Bone ingrowth is important for the long-term stability and success of an HTO, UKA, and TKA procedure. For bone ingrowth to occur, there must be a rough and irregular surface with pores for the bone to grow into. The optimal range of pore size for bone ingrowth is 100 to 400μm (Cross & Spycher, 2008). The implant being studied has a pore size of 150 μm. When it comes to initial stability, directly post-operative, this rough surface will increase the friction between the implant and the tibia (Cross & Spycher, 2008). Therefore, it will help provide additional initial stability for the implant by making it less easily mobile. Excessive micro-motion at the bone-implant surface can seriously

impact bone ingrowth from occurring. There should only be motion of 28-150μm. Any repeated motion higher than this could lead to only fibrous tissue growing into the implant (Cross & Spycher, 2008).

The porous coatings of implants conjure up a physiological response that is similar to bone healing. The process of ingrowth into a porous implant is similar to fracture healing in a stable situation. Similarly, a hematoma develops and becomes mesenchymal tissue. This tissue is then replaced by woven bone and then undergoes the same remodeling to normal bone structure. It differs by never going through the fibrocartilaginous formation stage. By the end of this, the porous spaces on the implant surfaces are filled with newly formed healthy bone tissue (Cross & Spycher, 2008).

The concept of bone "through-growth" has not commonly been studied in orthopedic research. Bone through-growth refers to bone growing through a space or "window" in an implant, instead of into the pores on the surface of an implant. There isn't currently a universally accepted word for this concept, so I will refer to it as through-growth for the purposes of this study. Certain osteotomy implants and spinal cages require through-growth for the long-term success of the procedure. The 4WEB Osteotomy Truss System is used for an Evans osteotomy of the foot to change the shape of the foot to correct a pes planus condition, also known as the flat foot condition ("Analysis of a Modified Evans Osteotomy", (n.d.)). Evans osteotomy procedures usually take around 6-8 weeks to heal. Three variations of the 4WEB implant can be seen below in **Image 3**. This implant system uses an open truss system to provide structural support for the osteotomy. Bone Graft is applied within the implant to encourage growth. The system allows the bone to grow through the osteotomy to eventually lead to the fusion of the bone after healing ("Osteotomy Truss System", (n.d)).

Image 4 4WEB Medical's Truss implant system ("Osteotomy Truss System", (n.d))

Spinal interbody cages (IC) also require through-growth for long-term surgical success. The purpose of spinal ICs is to restore lost intervertebral height and biomechanical stability. They achieve this through bone fusion. Similar variables are considered when designing ICs and when designing osteotomy implants. Maximum stability and optimized bone healing are the goals of both implants (Jain et al., 2016). Bone through-growth is necessary to achieve bone fusion for ICs. ICs contain spaces or windows that bone needs to grow through to achieve clinical success.

Bone through-growth is expected to occur in a very similar manner to the way fracture healing happens. This study will explore how different amounts of through-growth may affect the stability of the implant in the first 8 weeks after surgery.

2.8 Hypothesis:

This preliminary study explores how the addition of a window and the radius of curvature of the edges of that window in an interpositional implant affects the stability of the implant in

situ. It is hypothesized that a sharp radius around the edge of such a window will increase the force necessary to extract a simple interpositional implant from a foam urethane construct, while the increased amount of "through-growth" will also increase that extraction force for a given edge radius.

CHAPTER 3: MATERIALS & METHODS

3.1 Experimental Testing: Specimen Fabrication

The physical implants used in this study were designed on Fusion 360 (San Francisco, CA). They were then fabricated by Scale Workspaces in New Orleans, LA. The designs were based on the general geometry of the MTOWI high tibial osteotomy implant (Pontius, 2020). They can be seen in **Image 5 (a) and (b)**. These images show the design of the implants. Both the implants have the same geometry except for the radius of curvature of the edges of the circular "window". This study tests the effect of changing that radius.

(a)   (b)
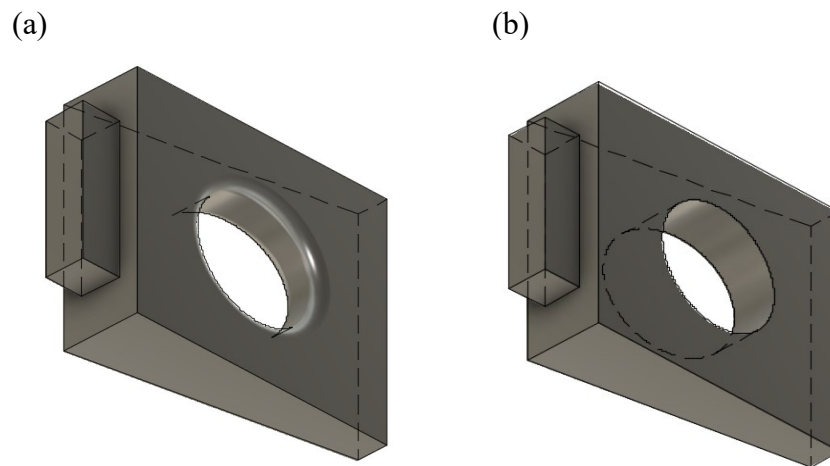
Image 5 Fusion360 files of two implant models (a) 2 mm radius of curvature on the edge of the circular window. (b) sharp, 0 mm radius of curvature

The implants were fabricated using Markforged Machines (Watertown, MA). The 3D printer, the Markforged Metal X Machine, initially made the parts using a 17-4 PH stainless steel and wax powder composite. This part was initially 30% larger than the final product and rested on a support tray. The part was then placed in the Wash-1 machine and washed using Opteon SF-79. This removed the first stage of the wax material. After being washed, the part was placed in Sinter-2. Sinter-2 took the part from being a lightly bound metal powder to a fully formed, solid metal part. The remaining wax was removed. The metal was sintered to form a uniform solid now the correct size; 30% smaller than when it was initially printed. The wax holding the part to

the support structure remained in powder form. It was easily removed by mechanical means, leaving the dimensionally accurate final part.

Rigid polyurethane foam (closed-cell, 20 pcf, Sawbones) was used to simulate the osteotomy site in the proximal tibia. The foam was purchased from SawBones (Vashon, WA). Sawbones is the industry standard for orthopedic test mediums. The foam blocks are an accurate alternative to cadaveric bone testing. This type of foam represents cancellous bone. Each trial for experimentation required two foam blocks to hold the implant: one straight and one angled block to match the implant geometry. Four types of foam block pairs were created to sandwich the two types of implants and to simulate different points in time during the healing process after the HTO procedure. For the 2 mm radius of curvature implant, foam blocks with a matching 2 mm radius at the curved through-growth junction were constructed. For the sharp zero-radius implants, foam blocks with a matching no-radius edge of through-growth were created. This design was intended to simulate how bone might grow into the implant in a clinical situation, following the shape of the implant. Two points in time post-operatively were also simulated using different foam block pairs. To represent the interface immediately after surgery, foam blocks were created with no through-growth. To represent hypothetical tissue growth into the window at about 8 weeks post-operative, foam blocks were machined with a 2 mm deep ring of foam from the block surface into the circular window (**Image 7).**

The foam pieces were constructed using closed-cell foam, 20 PCF, and 40 mm thick blocks. The blocks were designed to fit in test fixtures for an ADMET machine. The Fusion360 models are seen below in **Image 7 (a) and (b).** They were created using a ShopBot CNC machine (Durham, NC) to provide the right shape. **Image 6** shows one block being cut using the ShopBot machine at Scale Workspaces.

Image 6 ShopBot CNC machine used to cut foam blocks
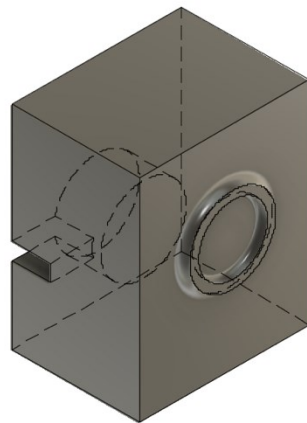
(a)   (b)
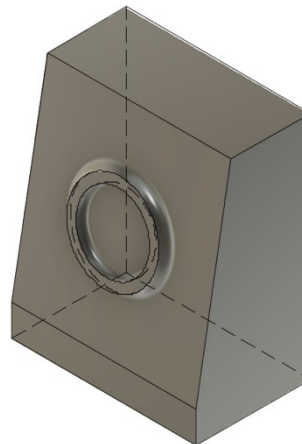
Image 7 Curved through-growth blocks, showing the contact surfaces and radiused through-growth rings
(a) straight block showing a hole intended to seat a button load cell (later abandoned) (b) angled block

To reiterate, the purpose of these pieces was to simulate the proximal tibia and act to

sandwich the implant in compression for mechanical testing. The final blocks were precisely

machined at Scale Workspaces and can be seen in **Image 8 (a) and (b)** below, positioned with

the implant. Note that the blocks each have a protruding ring of foam contacting surface that

represents the through-growth into the implant. The radii of curvature on the rings correspond to their matching implants.

(a)   (b)
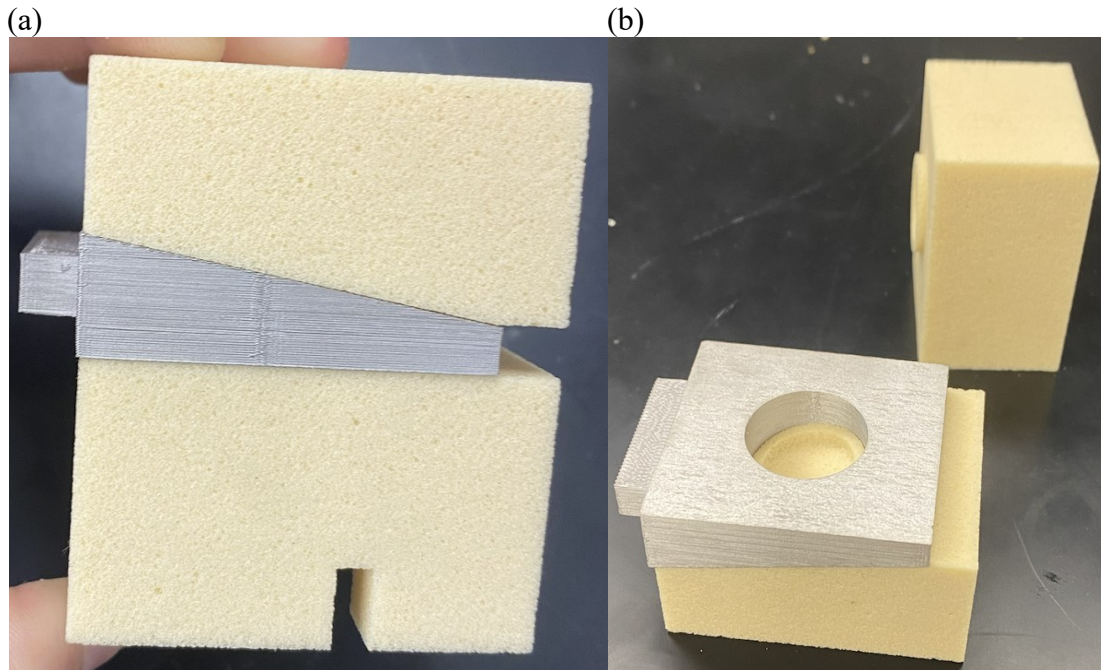
Image 8 Sharp foam blocks and implant assembly (a) assembled (b) disassembled. Note that the assembly corresponds to an interpositional implant within a wedge osteotomy site.

A problem with the initial design was noted after the first round of preliminary testing: the foam block and implant assembly slips within the ADMET testing fixtures. To correct this, linear ridges were milled into the outward-facing surfaces of the foam blocks. This was successful and held the assembly within the fixture to complete the testing. This proved an acceptable method of securing the block-implant construct in place.

3.2 Experimental Testing: Extraction Testing

Mechanical extraction testing was performed using an ADMET test frame and MTESTQuatro advanced testing system (Norwood, MA). The test setup is pictured below in **Image 9**. It is important to note that the direction of extraction was decided based on the assumption that the relationships between varying models would be consistent because the

extraction force is largely based off the interfaces between bone and implant and the compression acting on both. The block/implant assembly within an ADMET test fixture clamp can be seen in this image. The purpose of this clamp is to both hold and compress the assembly together and simulate interpositional placement. For each radius of curvature value, the following steps were repeated. The blocks were placed in the lower clamp attachment of the ADMET machine. The upper clamp was then attached to the ADMET, and the implant was placed within the clamp. The implant had to be tightened into the upper clamp, glue was used to ensure it stayed in place. The glue had no significant impact on results as it was used to keep the implant connected to the upper clamp for extraction. The upper clamp, connected to the implant, was lowered into the lower clamp. The lower clamp was then tightened to achieve an appropriate compression value of 50 lbs. The change in width of the test assembly was recorded to keep compression constant throughout all trials. This was recorded as the width difference in the results. It provides information on the tightness of the clamp. The ADMET machine was calibrated and zeroed before beginning the testing. A tension test using the MTESTQuatro software was performed in ramp loading mode at 1 mm/sec. Data from the real-time plot was collected. The plot provided time in seconds, load in kilograms, and position in millimeters. The maximum load was set to 200 kg. Displacement was used as a control variable.
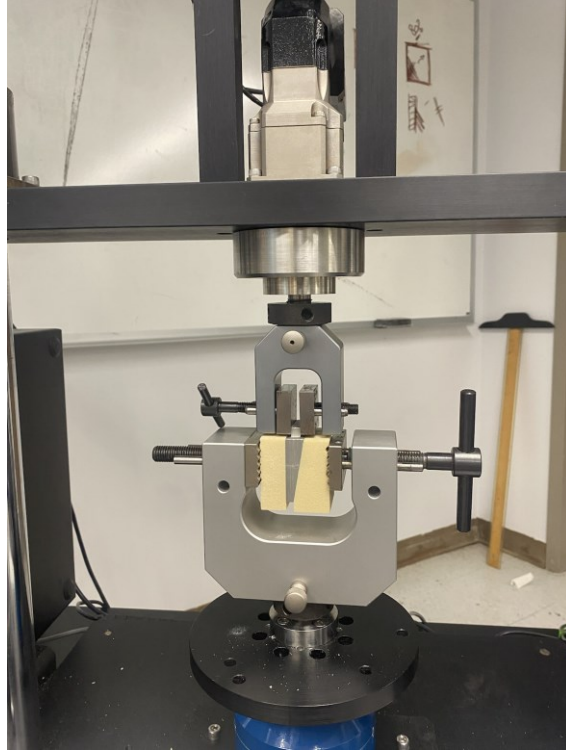
Image 9 Test setup on ADMET machine

3.3 Simulation: Component & Assembly Design

A computational model and simulation were created in Abaqus v2020 to replicate and

verify the experimental testing. The Fusion360 design files used to make the physical implants

were also used for the simulation. These files were imported from the Fusion360 to Abaqus FEA

software (Velizy Villacoublay, France). The implant was assigned material properties of

stainless steel including a Young's modulus of 197 GPa, a Poisson's ratio of 0.27, and a tensile

strength of 215 MPa. The blocks were assigned a Young's modulus of 247 MPa. The modulus of

20 pcf foam is 210 MPa in compression and 284 MPa in tension, an average of these values was

used under the assumption of isotropic material symmetry (Sawbones USA, 2022). The parts

were then seeded at 0.2 mm, and each piece was meshed using a tetrahedral shape. General

contact was assured, and coefficient of friction values for the interaction between the implant and

blocks were parametrically varied at 0.2, 0.4, and 0.8. A compression boundary condition on the

blocks held the implant in place, as were multidirectional constraints placed on the blocks to control movement. A boundary constraint of 0.02 mm displacement was placed on the left block towards the fixed right block to create pre-tightened compression. A small displacement was then placed upwards on the implant to achieve a tight fit for the through-growth region within the window. Then, various vertical forces were applied to the implant to find the maximum allowed force before failure. Failure load was defined at the point when the implant model began to move (Abaqus could not converge).

While completing the simulation using Abaqus FEA software, the friction and the forces acting on the implant were parametrically varied. This was done to find the minimum force required to extract the implant and fracture the urethane foam blocks. The testing was done for coefficients of friction values 0.2, 0.4, and 0.8. This was done on four analysis approach models. Model 1 included the implant with a curved radius at the window, and blocks that included through-growth. Model 2 included the implant with a curved radius at the window, and blocks without through-growth. Model 3 included the implant with a sharp radius of curvature on the edge of the window, and blocks with through-growth. Model 4 included an implant with a sharp radius of curvature and blocks without through-growth.

The goal of the simulation was to find the amount of force predicted to pull the implant out of the foam block sandwich construct, and then to compare these values with experimental results in order to develop failure criteria useful for future implant design.

In the case of a window with through-growth, experimentally observed to result in material failure, a modified Coulomb-Mohr criterion was assumed. The modified Coulomb-Mohr failure theory is commonly employed for brittle materials under combined stresses where the compressive strength exceeds tensile strength (Budynas et al., 2008). This is the case for 20

pcf closed-cell urethane foam. The manufacturer of the material reports shear, tensile, and compressive strengths of 20 pcf foam to be, respectively, 4.3 MPa, 5.6 MPa, and 8.4 MPa (Sawbones USA, 2022). These values are consistent with a Coulomb-Mohr material.

The maximum von Mises was calculated, considered, and compared to 4.3 MPa to represent the shear failure criteria. Maximum tensile and compressive stresses were compared to 5.6 MPa and 8.4 MPa, respectively. Whichever of these criteria was first exceeded was considered to correspond to the calculated allowable force.

Procedural reasoning was as follows: stop the analysis when the maximum allowable mises stress equaled 4.3 MPa, then check to see if the maximum tensile stress had exceeded a value of 5.6 MPa, then check to see if the maximum compressive stress exceeded 8.4. if "no" to both, use the von Mises criterion to define allowable failure load. If "yes," reduce the applied load until either maximum normal stresses equal the reported strengths, then use this load value.

The failure criteria for trials without through-growth was based on the observation that implant motion did not cause material failure of the foam. In these cases, failure load was defined solely when the interfacial friction was overcome. Again, this was assumed to occur at the point when the implant began to accelerate, and the standard static analysis could not converge. A series of trial-and-error loads were performed to determine the maximum load at which each computational analysis converged (within an estimated 5-7% under-predicted). This was considered the maximum load that could be applied to the implant without extraction and was thereby considered the load at failure. Each of these maximum loads were then compared to the maximum loads from the experimental models and conclusions were drawn.

CHAPTER 4: RESULTS

4.1 Experimental Testing Results

Four models were studied during experimental testing: curved edge with no through-growth, curved edge with through-growth, sharp edge with no through-growth, and sharp edge with through-growth. Each trial resulted in implant extraction from the foam block assembly. The loads reached to extract the implant were recorded for each trial. Change in position was the control variable and can be seen in each real-time plot below. The average maximum loads for each model are 35.6 kg, 112.0 kg, 91.0 kg, and 103.6 kg for the four models respectively. The highest averages belong to the implants representing 8 weeks postoperatively with through-growth.

4.1.1 Model 1: Curved Edge with No Through-Growth

      The first round of experimental testing that was performed was for the implant with a 2 mm radius of curvature representing post-operative conditions with no through-growth. 3 trials were performed for this, and the maximum loads were recorded. For each trial, the difference in width before and after compression of the assembly was recorded.

Table 2 Results of experimental testing for Model 1 (Implant with curved edge and no through-growth

Trial #	Maximum Load in kg (N)	Width Difference (mm)
1	41.0 (402.1)	0.29
2	34.0 (333.4)	0.84
3	31.8 (311.9)	0.53
Mean	35.6 kg $\pm$ 4.8	0.55

      The mean value for the maximum load is 35.6 kg $\pm$ 4.8 in kilograms and 349.1 N $\pm$ 47.1 in newtons. There is a 13.5% variation in values, which is consistent with expectations for the sample size of 3. This is especially true considering there is a much wider variation in construct compression.

Trial 1

A steadily increasing load was applied upwards on the implant until a maximum load of

41.0 kg was reached. The maximum load was reached at 0.4 seconds. Under this load, the

implant began extraction from the assembly and was pulled up at a steady rate. The load quickly

returned to zero kgs as the implant slid, which is expected as maximum friction was overcome.

The straight foam block and angled foam blocks showed no signs of damage after trial as can be

seen in **Image 11**. The ring in the photographs was present before testing.

Image 10 Curved edge with no through-growth: Trial 1 Real-Time Plot

a) b)

Image 11 Microscope images for the curved edge with no through-growth: Trial 1 (a) angled block and
(b) straight block

Trial 2

A steady increase in load was applied upwards on the implant until a maximum load of 34 kg was reached. This can be seen in **Image 12**. The maximum load was reached at 0.8 seconds. Under this load, the implant began extraction from the assembly. The angled block also began moving upwards with the implant. The straight foam block and angled foam blocks showed no signs of damage after trial as can be seen in **Image 13**.

Image 12 Curved edge with no through-growth: Trial 2 Real-Time Plot

a)   b)

Image 13 Microscope images for the curved edge with no through-growth: Trial 2 (a) angled block and (b) straight block

Trial 3

A steady increase in load was applied upwards on the implant until a maximum load of

31.8 kg was reached, as seen in **Image 14**. The maximum load was reached at 0.9 seconds.

Under this load, the implant began extraction from the assembly. The straight foam block and

angled foam blocks showed no signs of damage after trial as can be seen in **Image 15**.
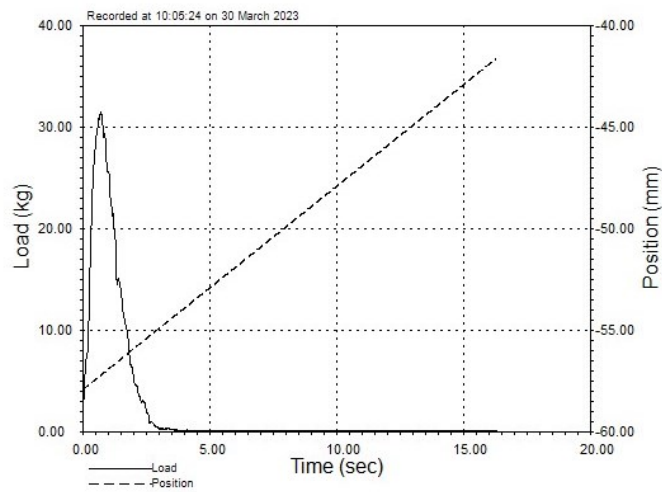
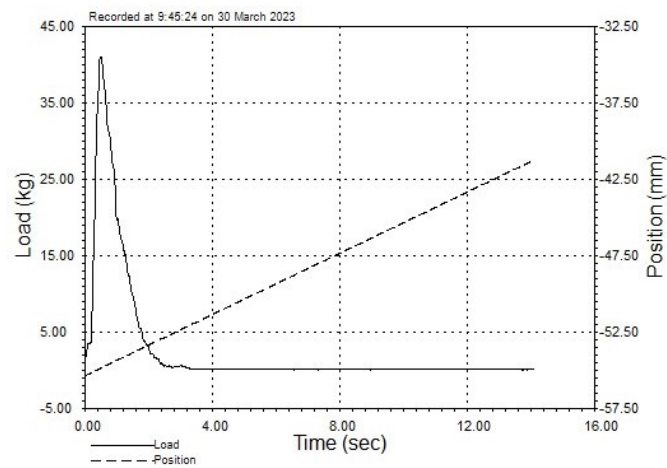Image 14 Curved edge with no through-growth: Trial 3 Real-Time Plot
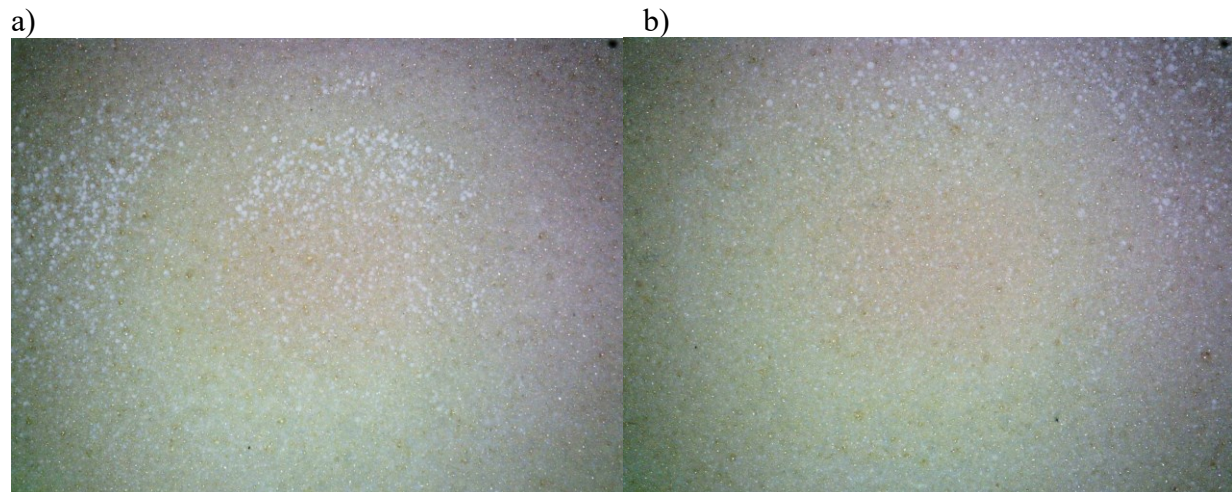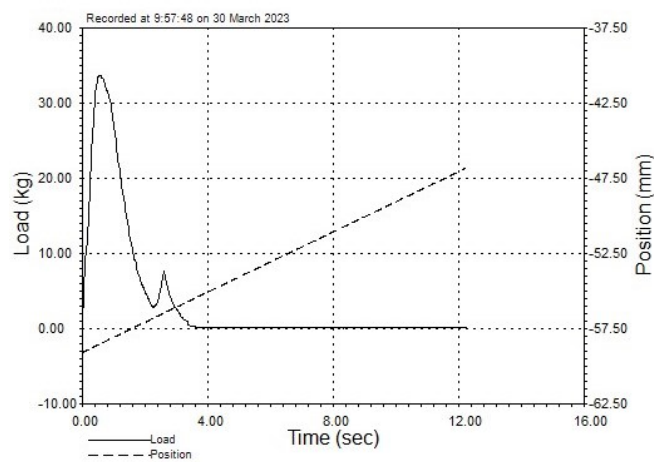
a)   b)
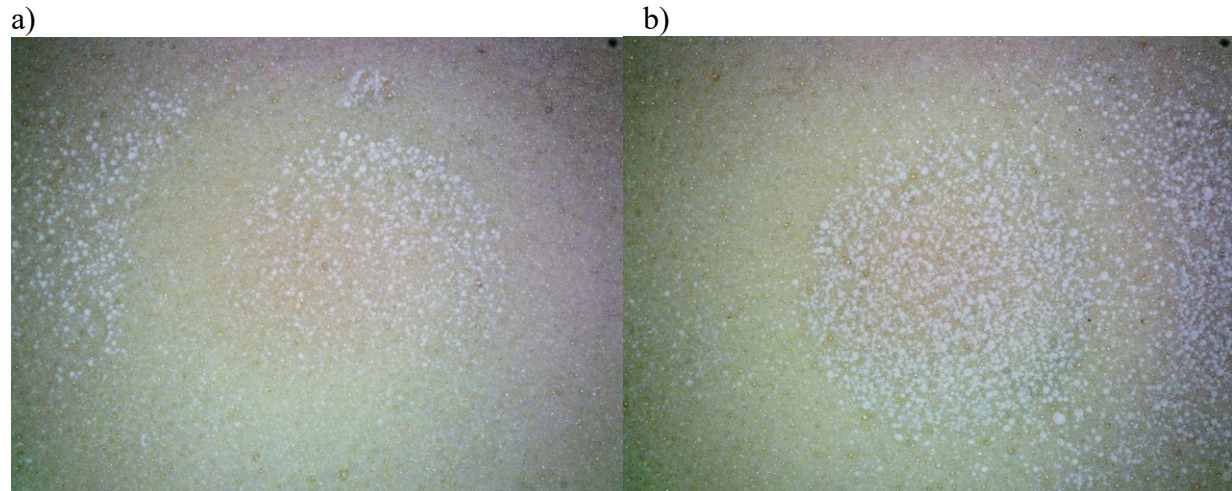
Image 15 Microscope images for the curved edge with no through-growth: Trial 3 (a) angled block and (b) straight block

4.1.2 Model 2: Curved Edge with Through-Growth

      The second round of experimental testing that was performed was for the implant with a

2 mm radius of curvature and 2 mm of through-growth representing about 8 weeks

postoperatively. 3 trials were performed for this and the maximum loads were recorded. For each

trial, the difference in width before and after compression of the assembly was recorded.

Table 3 Results of experimental testing for Model 2 (Implant with curved edge and through-growth)

Trial #	Max Load in kg (N)	Width Difference (mm)
1	100.0 (980.6)	0.41
2	108.0 (1059.1)	0.43
3	128.0 (1255.3)	0.25
Mean	112 kg $\pm$ 14.4	0.36

      The mean value for the maximum load is 112 kg $\pm$ 14.4 in kilograms and 1098.3 N $\pm$

141.5 in newtons. There is a 12.9% variation in values, which is consistent with expectations for

the sample size of 3. This is especially true considering there is a much wider variation in

construct compression. This extraction force with through-growth and a curved edge is

approximately 3 times greater than that without through-growth.

Trial 1

From **Image 16,** a steady increase in load was applied upwards on the implant until a maximum load of 100 kg was reached. The maximum load was reached at 3 seconds. Under this load, the lower part of the through-growth began to "fracture" or experience damage. The implant continued to be extracted and the through-growth continued to fracture until 24 seconds. This through-growth fracture can be appreciated as load fluctuation and relatively slow declining force between 10 and 24 seconds. The straight foam block and angled foam blocks lost about 70% of the through-growth during extraction. Note that the apparent width of the through-growth damage is larger than that before extraction. The lower parts of the ring appear partially crushed into the block, and the failure force graph is consistent with a porous specimen undergoing compression failure.

Image 16 Curved edge with through-growth: Trial 1 Real-Time Plot
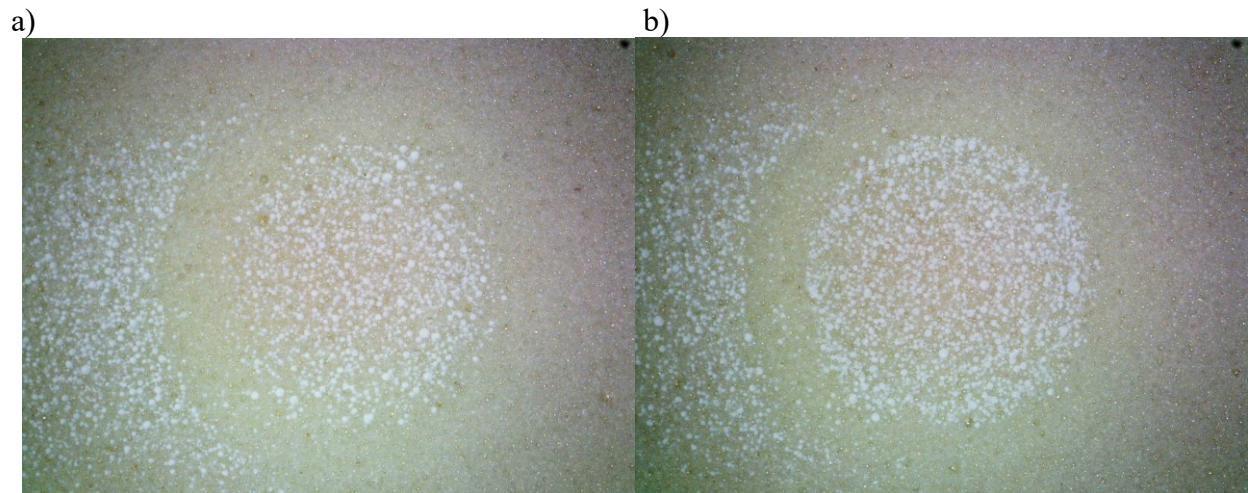
a)   b)

Image 17 Microscope images for curved edge with through-growth: Trial 1 (a) angled block and (b) straight block

Trial 2

A steady increase in load was applied upwards on the implant until a maximum load of 108 kg was reached as can be seen in **Image 18**. The maximum load was reached at 1 second. Under this load, the lower part of the through-growth began to fracture. The implant continued to be extracted and the through-growth continued to fracture until 22 seconds, as can be seen by the fluctuating load from 15 to 22 seconds. The majority of the through-growth ring came off on both the angled and straight foam blocks. Once again, the thickness of the through-growth ring increased after extraction as some of the crushed through-growth was pushed into the foam block. A small part of the upper through-growth was also separated from the block after testing. As with trial 1, the failure force graph shows characteristics of a crush damage mechanism for a porous material.
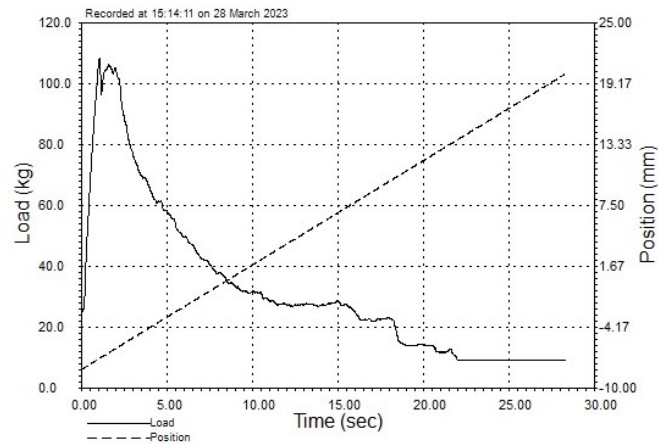
Image 18 Curved edge with through-growth: Trial 2 Real-Time Plot

a)   b)

Image 19 Microscope images for the curved edge with through-growth: Trial 2 (a) angled block and (b) straight block

Trial 3

A steady increase in load was applied upwards on the implant until a maximum load of 128 kg was reached. This can be seen in **Image 20** below. The maximum load was reached at 2 seconds. Under this load, the lower part of the through-growth began to fracture. The implant continued to be extracted and the through-growth continued to fracture until 23 seconds. This is evident from the fluttered section of the lines between 5 and 23 seconds. About half of the through-growth fractured on both foam blocks, which can be seen in **Image 21** below. Both

blocks had an increase in ring thickness. As can be seen in trials 1 and 2, characteristics of a

crush damage mechanism are evident in **Image 20.**

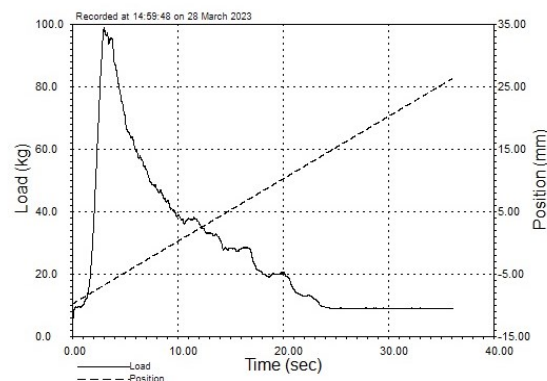Image 20 Curved edge with through-growth: Trial 3 Real-Time Plot
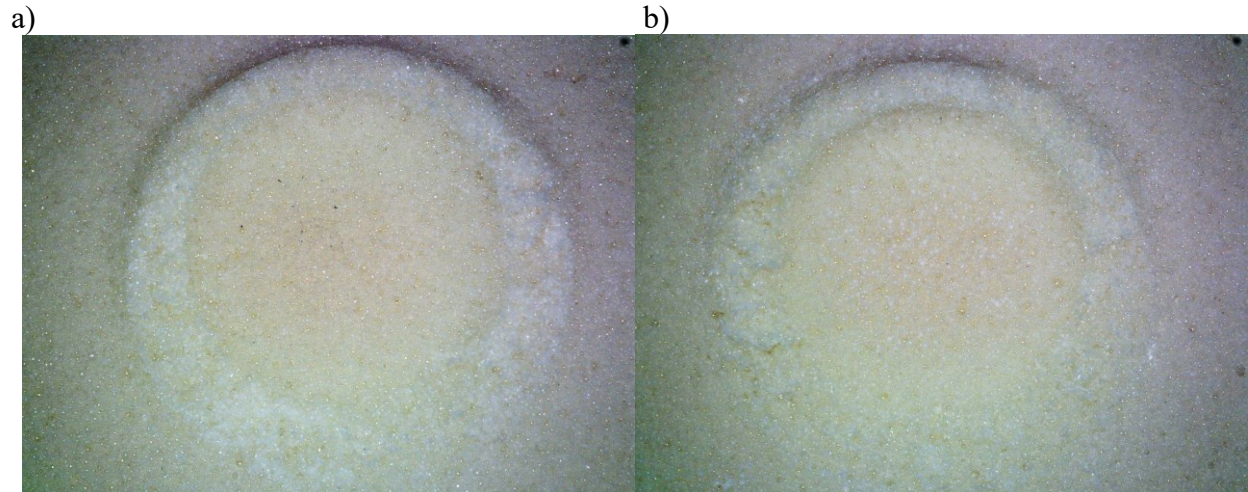
a)   b)

Image 21 Microscope images for curved edge with through-growth: trial 3 (a) angled block and (b)
straight block

4.1.3 Model 3: Sharp Edge with No Through-Growth

The third round of experimental testing that was performed was for the implant with a

sharp radius of curvature and under a post-operative scenario with no through-growth. 3 trials

were performed for this, and the maximum loads were recorded. For each trial, the difference in

width before and after compression of the assembly was recorded.

Table 4 Results of experimental testing for Model 3 (Implant with sharp edge and no through-growth)

Trial #	Max Load in kg (N)	Width Difference (mm)
1	55.0 (539.4)	0.63
2	106.0 (1039.5)	0.20
3	112.0 (1098.3)	0.58
Mean	91 kg $\pm$ 31.3	0.47

The mean value for the maximum load is 91 kg $\pm$ 31.3 in kilograms and 892.4 N $\pm$ 307.1

in newtons. There is a 34.4% variation in values, this more than twice as large as the variation in

the previous two models. This suggests that trial 1 may represent a mode of failure different than

that of trials 2 and 3. The width difference for Model 3 is not significantly greater than the width

differences for the previous two models.

Trial 1

A steady increase in load was applied upwards on the implant until a maximum load of 55 kg was reached, as seen in **Image 22** below. The maximum load was reached at 0.6 seconds. Under this load, the implant began extraction from the assembly. The load quickly returned to zero before 3 the second mark. The straight foam block and angled foam blocks showed no obvious signs of damage after trial as can be seen in **Image 23**. Note that the failure graph is, again, characteristic of a friction-mediated failure. As are the undamaged block surfaces.
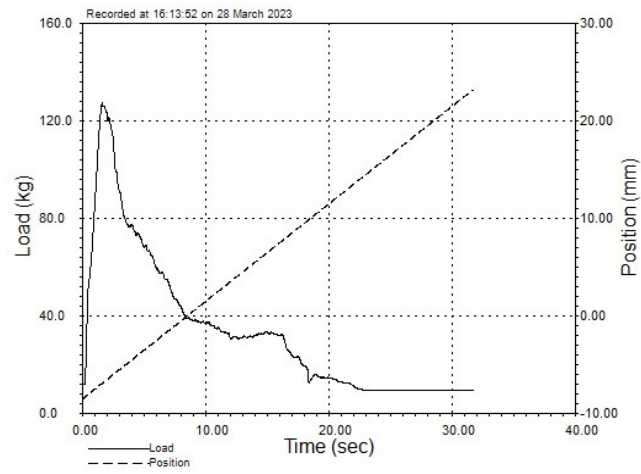

Image 22 Sharp edge with no through-growth: Trial 1 Real-Time Plot

a)   b)
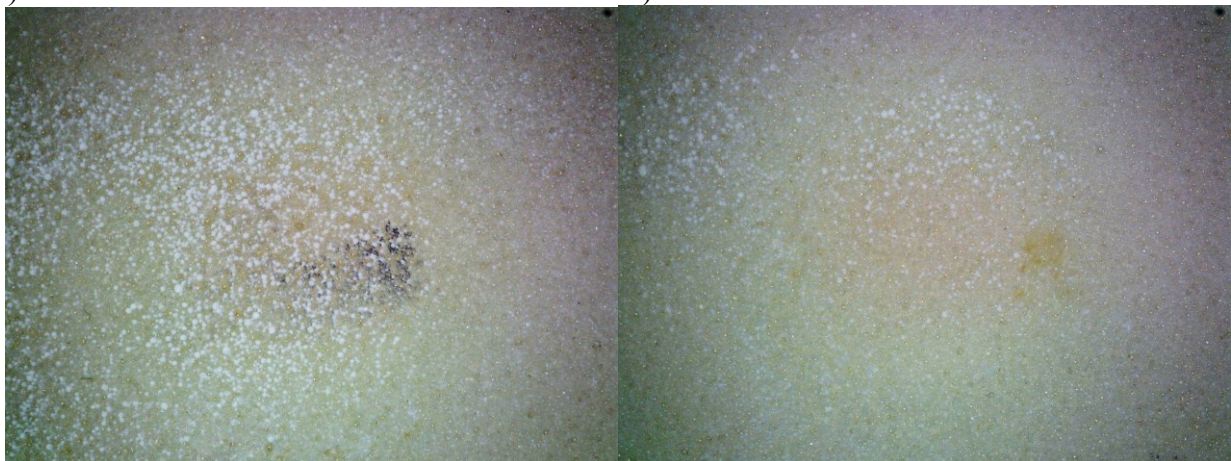
Image 23 Microscope images for sharp edge with no through-growth: Trial 1 (a) angled block and (b) straight block

Trial 2

In **Image 24** below, a steady increase in load was applied upwards on the implant until a maximum load of 106 kg was reached. The maximum load was reached at 1 second. Under this load, the implant began extraction from the assembly. The straight foam block and angled foam blocks showed no signs of damage after trial as can be seen in **Image 25**. The visible ring seen below was present before testing and is flush with the foam block surface. However, the failure force graph does display a more gradual decrease in load after peak failure. This suggests some damage beyond friction may be present, though not obvious on the magnified image.

Image 24 Sharp edge with no through-growth: Trial 2 Real-Time Plot

a)   b)
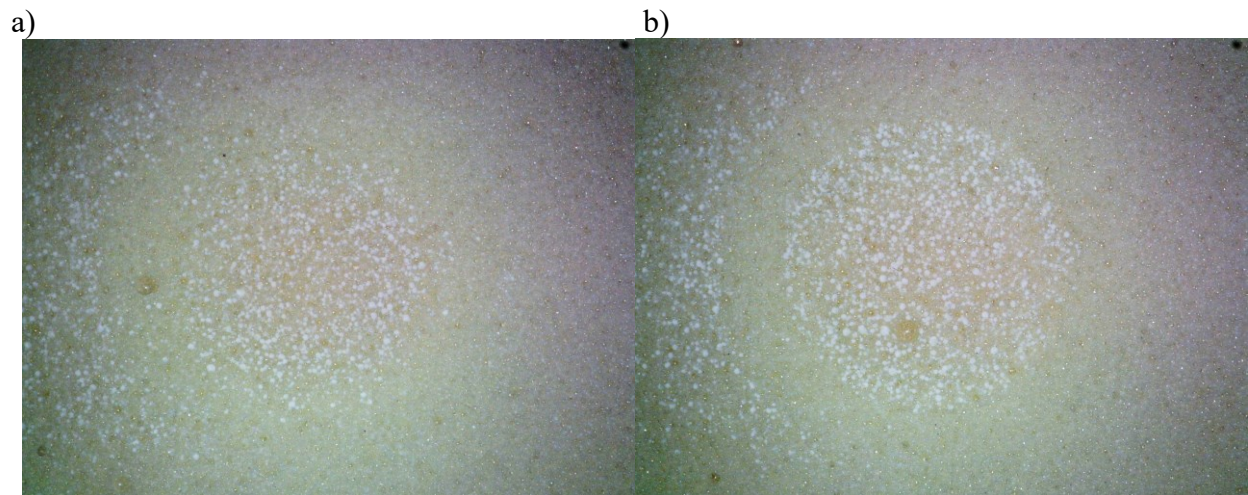
Image 25 Microscope images for sharp edge with no through-growth: Trial 2 (a) angled block and (b) straight block

Trial 3

A steady increase in load was applied upwards on the implant until a maximum load of 112 kg was reached. This can be observed in **Image 26** below. The maximum load was reached at 1 second. Under this load, the implant began extraction from the assembly. The straight foam block and angled foam block showed no obvious signs of damage after trial as can be seen in **Image 27**. However, as with trial 2, a region of suspected damage other than friction is again present.
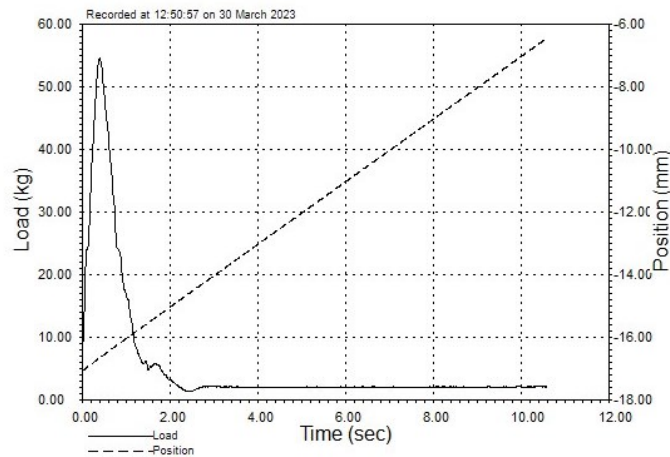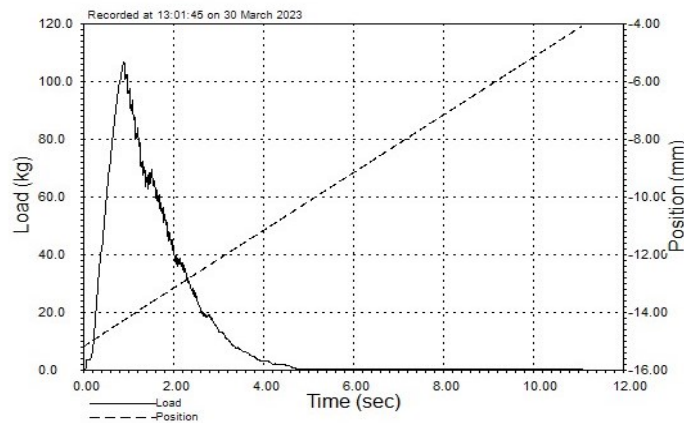

Image 26 Sharp edge with no through-growth: Trial 3 Real-Time Plot
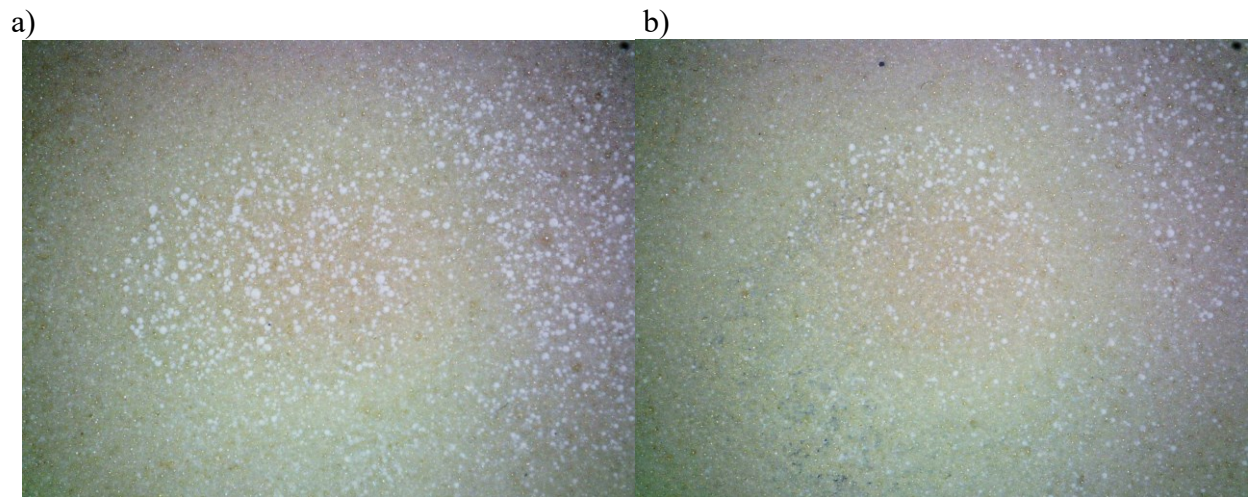
Image 27 Microscope images for sharp edge with no through-growth: Trial 3 (a) angled block and (b) straight block

4.1.4 Model 4: Sharp Edge with Through-Growth

The fourth round of experimental testing that was performed was for the implant with a sharp radius of curvature, representing 8 weeks post-operatively with through-growth. 3 trials were performed for this and the maximum loads were recorded. For each trial, the difference in width before and after compression of the assembly was recorded.

Table 5 Results of experimental testing for Model 4 (Implant with a sharp edge and through-growth)

Trial #	Max Load in kg (N)	Width Difference (mm)
1	95.0 (931.6)	0.15
2	98.0 (961.0)	0.08
3	118.0 (1157.2)	0.5
Mean	103.7 kg $\pm$ 12.5	0.73

The mean value for the maximum load is 103.7 kg $\pm$ 12.5 in kilograms and 1016.6 N $\pm$ 122.6 in newtons. There is a 12.1% variation in values. This variation for Model 4 is comparable to Models 1 and 2 and is consistent with what one might anticipate for a small sample size. It is noteworthy that Model 3 displayed a range of variation 2 times that of all other models. This may imply that the presence of a mixed failure mode may be the source of increased variability of results.

Trial 1

A steady increase in load was applied upwards on the implant until a maximum load of 95 kg was reached. The maximum load was reached at 1.6 seconds. Under this load, the lower part of the through-growth began to fracture. The implant continued to be extracted and the through-growth continued to fracture until 14.4 seconds. This can be seen by the fluctuating portion of the load line in **Image 28**. About 60% of the through-growth on the angled block was

fractured off, but only about half of the through-growth on the straight block was fractured. Parts of the foam block underneath the through-growth surface also appeared to have been peeled off, as can be seen on both blocks (a) and (b), indicating some complex mode of tensile failure. The failure force graph does not return to zero force quickly but shows a gradual, nonuniform descent towards no load.
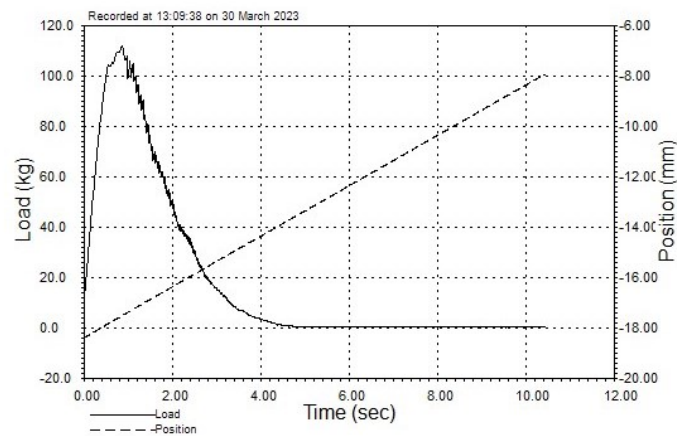

Image 28 Sharp edge with through-growth: Trial 1 Real-Time Plot

a)   b)

Image 29 Microscope images for sharp edge with through-growth: Trial 1 (a) angled block and (b) straight block

Trial 2

A steady increase in load was applied upwards on the implant until a maximum load of 99 kg was reached. The maximum load was reached at 2 seconds. Under this load, the lower part of the through-growth began to fracture. The implant continued to be extracted and the through-growth continued to fracture until 18.25 seconds. Almost all of the through-growth on the angled block (block (a)) was fractured off but less than half of the through-growth on the straight block (block (b)) was fractured. On blocks (a) and (b), some of the material underneath the through-growth appeared to tear or peel. The ends of the remaining through-growth rings in block (b) both have fractures around the interface between the foam block body and the through-growth structure. Furthermore, the damage surface does not display the widening seen in Model 2, thought to show characteristics of a crush or compression failure.
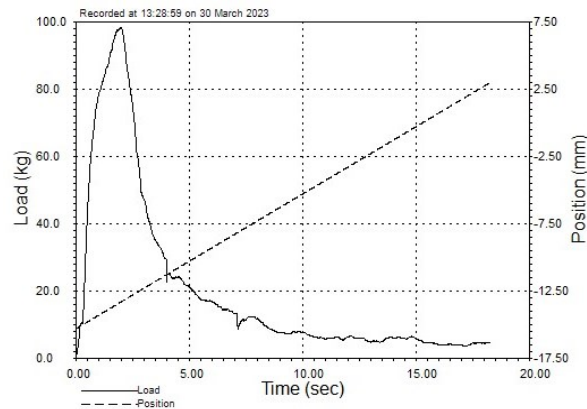
Image 30 Sharp edge with through-growth: Trial 2 Real-Time Plot

a)   b)
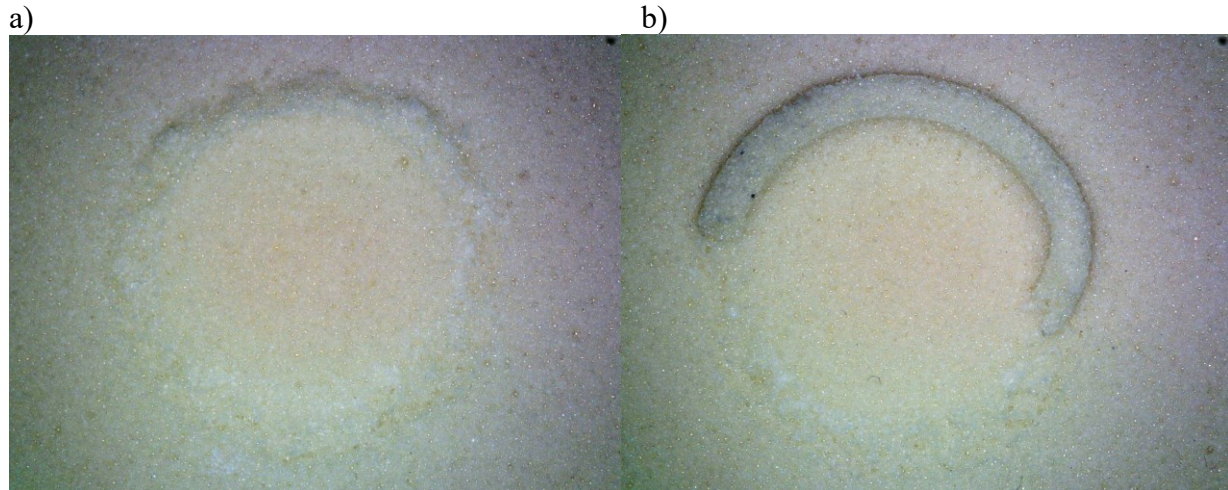
Image 31 Microscope images for sharp edge with through-growth: Trial 2 (a) angled block and (b) straight block

Trial 3

From **Image 32,** a steady increase in load was applied upwards on the implant until a maximum load of 118 kg was reached. The maximum load was reached at 0.4 seconds. Under this load, the lower part of the through-growth began to fracture. The implant continued to be extracted and the through-growth continued to fracture until 12.4 seconds. This can be seen by the minor fluctuations in the load line. About 80% of the through-growth on the angled block was removed, as can be seen in **Image 22**. About 90% of the through-growth on the straight block (**Image 33 block (b)**) was removed. About 70% of the through-growth on the angled block was removed, as well as some underlying material from the foam block body that has been torn or peeled, reinforcing the manner of tensile failure. The load line does not return to zero rapidly.
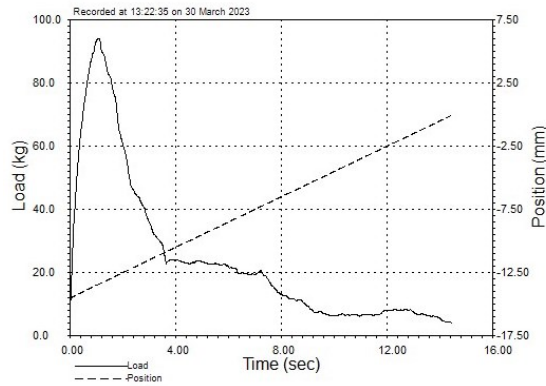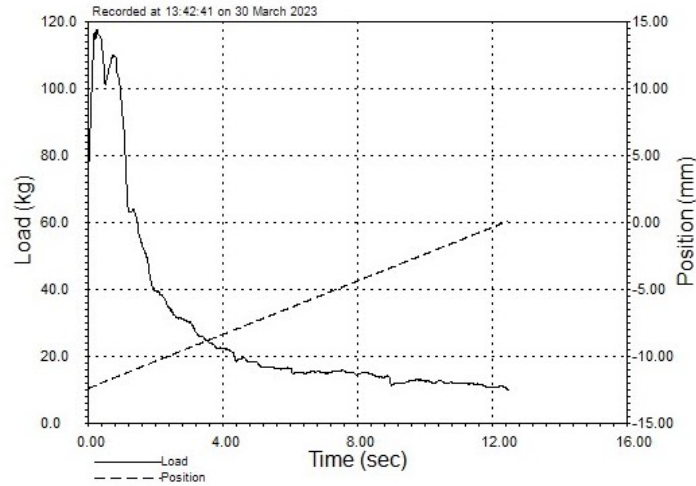
Image 32 Sharp edge with through-growth: Trial 3 Real-Time Plot

a)   b)
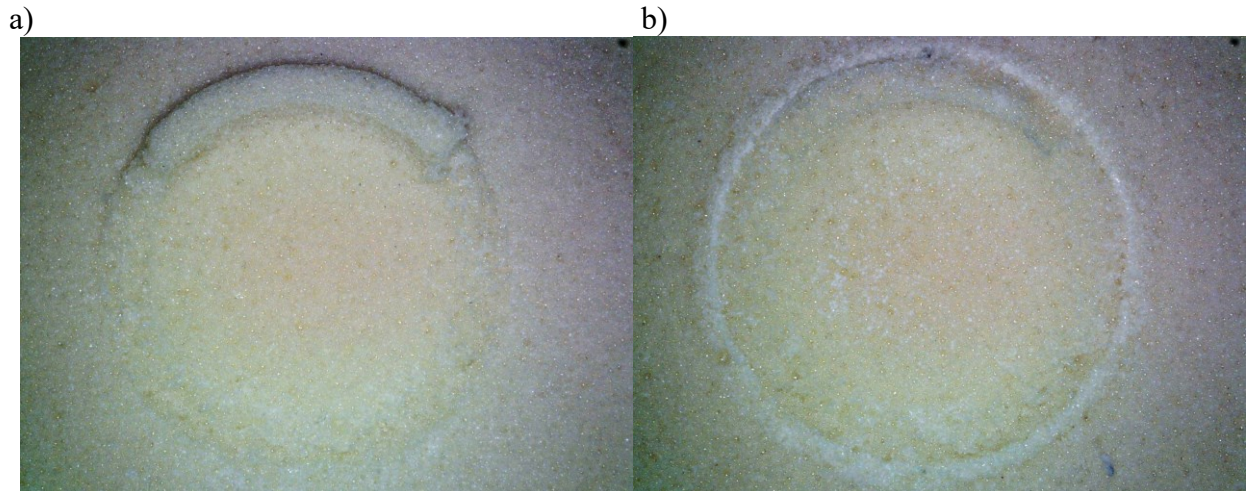
Image 33 Microscope images for sharp edge with through-growth: Trial 3 (a) angled block and (b) straight block

4.2 Simulation Testing Results:

      The tables below present a summary of the collected data from the computational testing.

Table 6 presents the maximum load in Newtons for the two types of implant edges at three

different coefficients of friction (0.2, 0.4, 0.8) at T=0 with no through-growth. The load values

increase linearly for both types of implants with the increase of friction. The sharp edge implant

can withstand higher loads at all three coefficients of friction compared to the implant with the

curved edge.

Table 6 Overall results of simulation testing for models without through-growth (T=0)

Implant Type	Maximum Load (N) with Coefficient of Friction= 0.2	Maximum Load (N) with Coefficient of Friction= 0.4	Maximum Load (N) with Coefficient of Friction= 0.8
Sharp Edge	295.0	795.0	1560.0
Curved Edge	16.0	40.0	90.

Table 7 shows the overall maximum load in Newtons for the same two types of implants at the same coefficients of friction but with through-growth at T=1. Again, the sharp edge implant can withstand higher loads at all three coefficients of friction compared to the curved edge implant. However, the maximum loads for both types of implants are generally higher in this table compared to the first table. The sharp edge implant maximum loads increase linearly with the increase in friction. The maximum loads for the curved edge implant do not increase with friction the way that the sharp edge implant does. The maximum load for the curved edge stays fairly constant as friction increases.

Table 7 Overall results of simulation testing for models with through-growth (T=1)

Implant Type	Maximum Load (N) with Coefficient of Friction= 0.2	Maximum Load (N) with Coefficient of Friction= 0.4	Maximum Load (N) with Coefficient of Friction= 0.8
Sharp Edge	410.0	902.0	1520.0
Curved Edge	92.0	88.0	91.0

Von Mises stress serves as a measure to assess if a material will yield or fracture. According to the von Mises yield criterion, if the von Mises stress experienced by a material

under a load reaches or exceeds the yield limit of that material, the material will yield (SimScale, 2023). The yield limit of the foam blocks is 4.3 MPa. A uniform color map in **Image 34** below acts as a key to qualitatively evaluate the result images for failure. This color map has a range from 0 to 6 MPa. The yield limit of 4.3 MPa corresponds to the yellow color on the map. Any yellow, orange, red or grey shown on the foam blocks represent failure and extraction. Maximum principal stress and minimum principal stress were also observed for each trial to support the conclusion that the material would not yield. Maximum principal stress is a failure predictor for multiaxial stress systems. If the maximum principal stress reaches the failure value anywhere within the object, the object will fracture (Todinov, 2007). The maximum principal stress value for the foam block is 5.6 MPa. The minimum principal stress value for the foam block is 8.4.

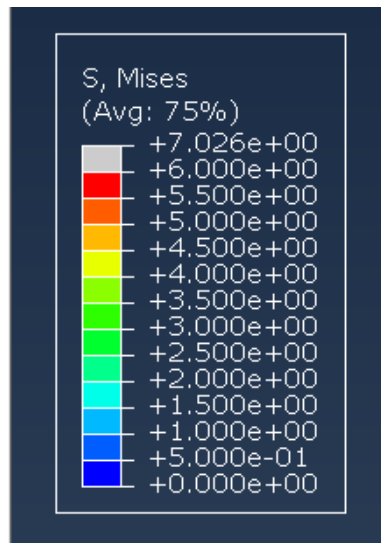Image 34 Color Map of von Mises stress in MPa

Image 35 shows the results of all four models: curved edge without through-growth, sharp edge without through-growth, curved edge with through-growth, and sharp edge with through-growth at their maximum loads with a coefficient of friction of 0.2. These loads are 16 N, 295 N, 92 N, 410 N respectively. The two models without through-growth show little to no

von Mises stress as these blocks do not fracture at extraction. In order for extraction they need to surpass the friction acting between the implant and the foam blocks, therefore it makes sense how the maximum load values increase linearly as the friction increases. The curved edge without through-growth model shows 0 von Mises stress acting on the foam block. The sharp edge without-through growth model shows between 1 and 1.5 MPa on von Mises acting on the foam blocks mainly at the interaction points between the foam blocks and implant. As the yield strength of the material is 4.3 MPa, the blocks will not fracture in this state. Maximum and Minimum principal stresses were also observed to support this data, and the foam blocks did not reach those limit values. The two models with through-growth had significantly higher von Mises stress values. The stress on the model is concentrated at the outermost edge of the bottom point of the through-growth. This is where the implant begins pushing up on the through-growth and applies the most pressure at the beginning of extraction. The two models with through-growth experienced 4.2 MPa in this area.

Image 36 shows the results of all four of the models with a coefficient of friction value of 0.4. As the friction increased, values of maximum load increased for all models except the curved edge with ingrowth. The curved edge model without through-growth had again little to no von Mises stress acting on the foam blocks and a maximum load of 40 N. The sharp edged model with no through-growth had between 1.5 and 2 MPa acting on the regions with the highest stress concentrations. It had a maximum load of 795 N which is almost 20 times the maximum load of the curved implant. The models with ingrowth both had 4.2 MPa acting on the areas with the highest stress concentrations. The curved model had a maximum stress of 88 N and the sharp model had a maximum load of 902 N.

Image 37 presents the results of all four models with a 0.8 coefficient of friction value. With this increased coefficient of friction, the maximum loads for both the models without through-growth and the sharp model with through-growth. The maximum value for the curved model with through-growth stays around the same value for each increase in friction. The curved edge model with no through-growth again has 0 von Mises stress acting on the foam blocks. The sharp edge model with no through-growth has 3 MPa acting on the foam block. The curve edge model and sharp edge model with through-growth have 4.2 MPa acting on the foam block in the areas with the highest stress concentrations.

Image 35 Computation results of von Mises stress for 0.2 value of coefficient of friction in isometric view comparing: (a) curved edge without through-growth from maximum load of , (b) sharp edge without through-growth, (c) curved edge with through-growth, (d) sharp edge with through-growth.
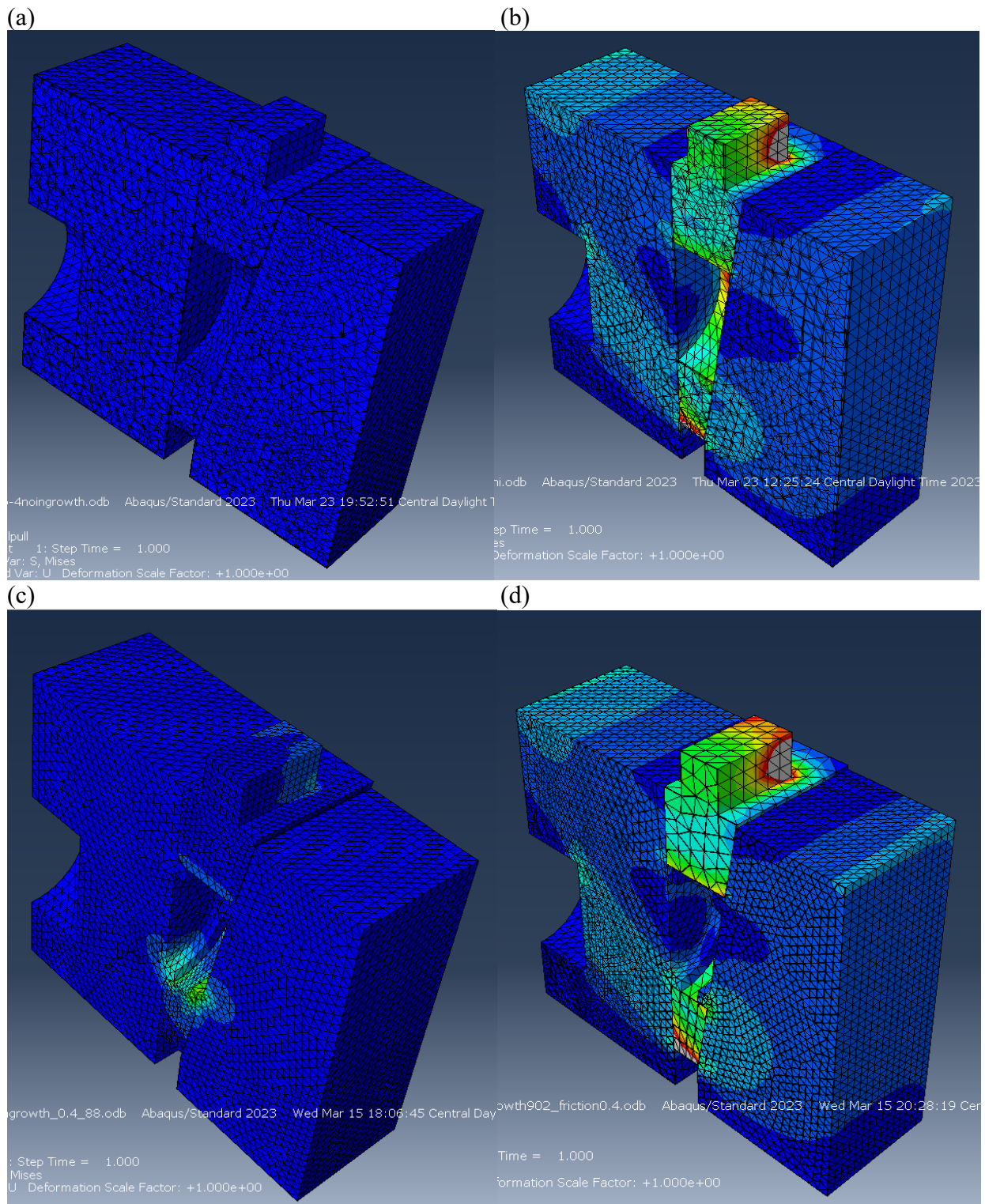
Image 36 Computation results of von Mises stress for 0.4 value of coefficient of friction in isometric view comparing: (a) curved edge without through-growth, (b) sharp edge without through-growth, (c) curved edge with through-growth, (d) sharp edge with through-growth.
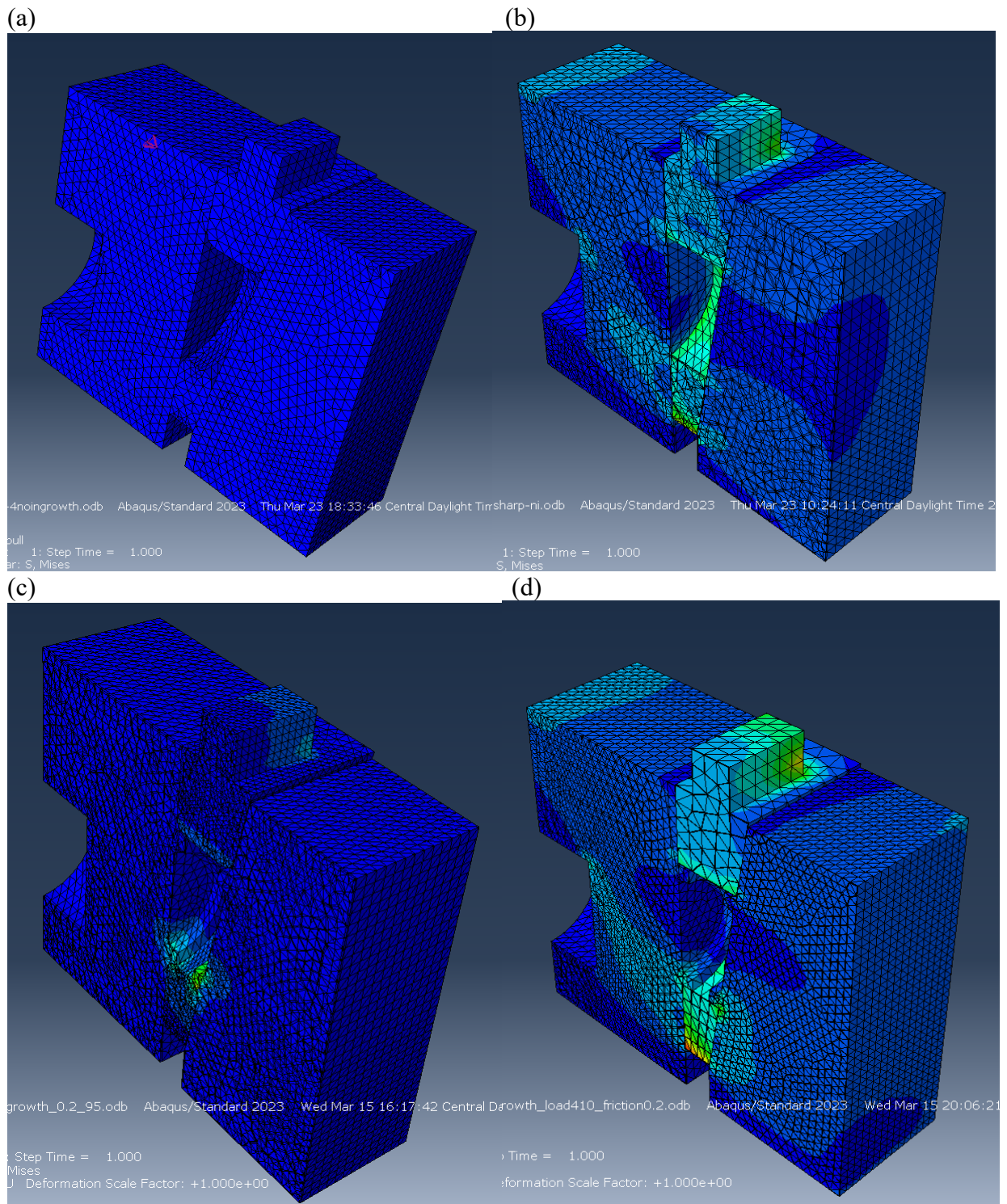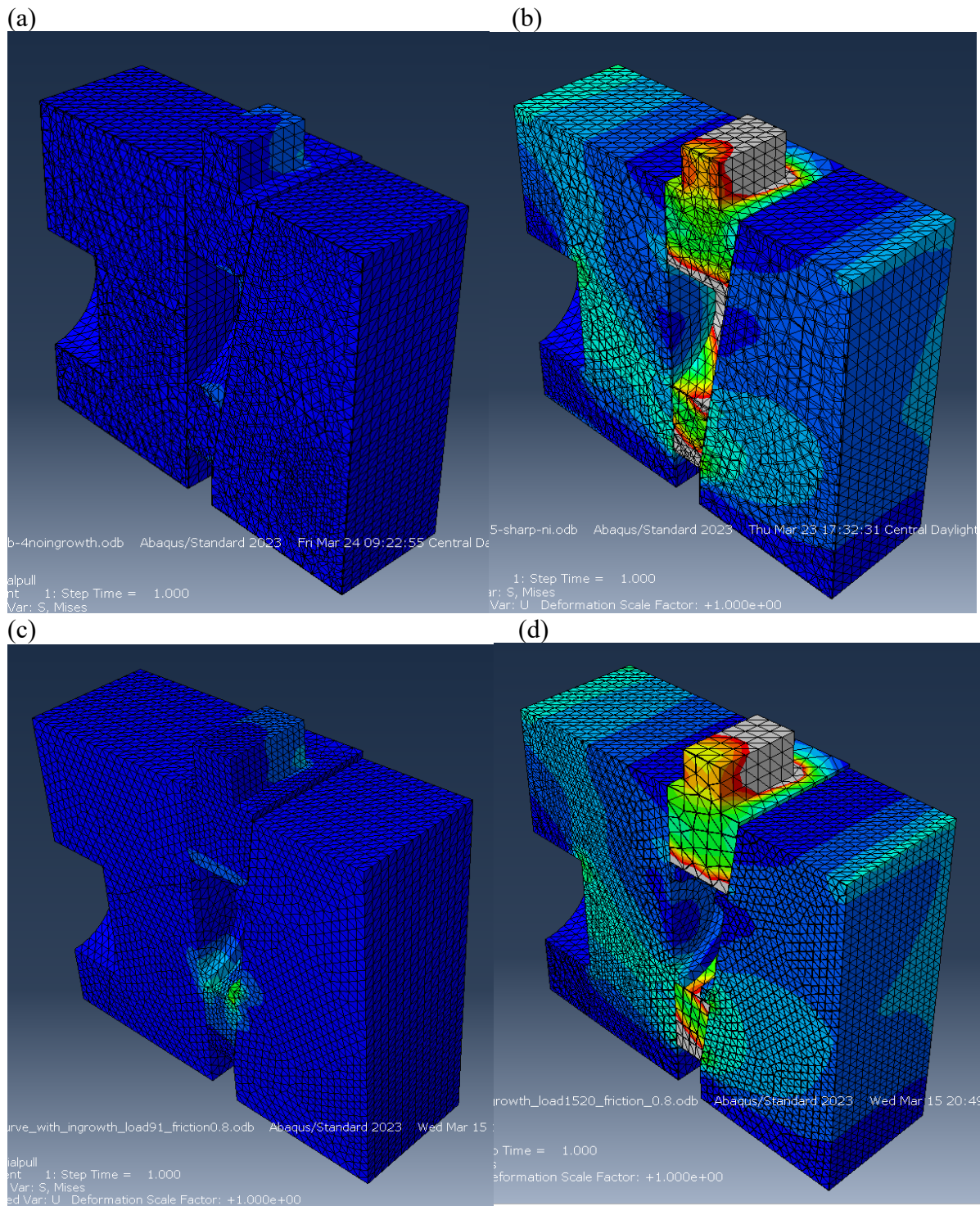
Image 37 Computation results of von Mises stress for 0.8 value of coefficient of friction in isometric view comparing: (a) curved edge without through-growth from maximum load of , (b) sharp edge without through-growth, (c) curved edge with through-growth, (d) sharp edge with through-growth.

Different areas of the foam blocks experience different amounts of stress. Throughout all the through-growth models, the area with the highest stress concentration is on the outermost edge of the bottom point of the through-growth on the angled foam blocks. The angled foam blocks were consistently where the failure occurred first. The area with the second highest stress concentration was the same location on the straight foam block. The sharp foam blocks also experienced high-stress concentrations at the upper corner of the through-growth areas. Overall, the sharp edge models had the highest maximum loads for both the models with and without through-growth. The sharp edge models' maximum values were consistently at least 4 times the corresponding curve edge value. All the models except for the curved edge model without through-growth had an increase in maximum stress with an increase in friction.

CHAPTER 5: DISCUSSION & CONCLUSION

5.1 Experimental Testing

In this study, extraction testing was used to determine the effect of varying the radius around the window and the amount of through-growth into that window. The maximum load values represent the amount of load required to extract the implant from the assembly. The first trials focused on an implant with a curved radius and no through-growth. The zero through-growth models represent how the implant acts directly after surgery when no bone ingrowth or through-growth has occurred. In each of these trials, the maximum load was reached in less than 1 second, and the maximum load returned to zero rapidly after as the implant slides. The results showed the lowest maximum loads of all the trials. It is predicted that the load was primarily mediated by the friction acting between the implant and block surfaces. The average maximum load for these trials was calculated to be 35.6 kg $\pm$ 4.8. This is significantly lower than the sharp radius without through-growth which had an average maximum load of 91.0 kg $\pm$ 31.3. This suggests that the sharp radius implant has the ability to catch onto the surface of the foam block, whereas the curved radius slides off the surface more easily. The sharp radius also had a wider range of maximum loads for each trial: 55.0 kg, 106.0 kg, and 112.0 kg. The range is 57.0 kg for the sharp radius and only 9.2 kg for the curved radius. This is a 34.4% variation in values for the sharp radius and 13.5% variation for the curved radius. The variation for the curved radius implant is consistent with expectations for a sample size of 3, especially considering the much wider variance in width difference from those trials. The width difference for the sharp radius is smaller than for the curved radius. This suggests that the larger variation may be due to the implant with a sharp radius catching on surface imperfections and irregularities of the block. During Trial 1 the sharp edge implant had a maximum load of 55 kg, this is closer to the load

values for the curved edge than for the rest of the values for the sharp edge. The load failure

graph also follows the patterns of the curved edge implant without through-growth. This pattern

and the lack of damage to the foam block surfaces are characteristic of a friction-mediated

failure. Trials 2 and 3 suggest damage other than friction is present. That is suggested by the load

fluctuations shown after initial extraction force and the fact that load does not quickly fall back

to zero. The implant appears to be catching on the imperfections on foam block surfaces. This

could imply that the quality of the cut surface may have an impact directly after surgery. If the

sharp edge is catching on imperfections, then a surgeon may want to use a coarser surgical saw

when making the incision into the tibia. This would lead to a less smooth surface for the implant

to catch onto and more initial stability post-operatively. In this case, surface imperfections on the

cut surface of the tibia would be beneficial. It is important to note that even though a coarse

surface could be beneficial for stability, a surgeon wouldn't want too irregular of a cut which

may lead to some movement of the implant within the surgical site. Another surgical implication

of this result is that making the sides of the implant slightly concave in the bone could also lead

to more initial stability. The concavity could also dig into the bone, providing this stability.

The next two setups to be compared are the implant with a curved radius with 2 mm of

through-growth and the implant with a sharp radius and 2 mm of through-growth. The curved

radius with through-growth had an average maximum load of 112.0 kg $\pm$ 14.4 and a variation of

12.9%. It is important to note that the maximum force graph is consistent with expectations for a

porous specimen undergoing compression failure and crush damage mechanism. The sharp

radius with through-growth had an average maximum load of 103.7 kg $\pm$ 12.5 and a variation of

12.1. The maximum load graphs show a gradual nonuniform descent. The values comparing

curved edge versus sharp edge are much closer together for through-growth than without

through-growth. This implies that at the point in time where 2 mm of through-growth has grown (about 8 weeks post-operatively) that the stability of the implant is much less dependent on the factor of edge radius.

The variation in model 4 is comparable to models 1 and 2 and consistent with expectations for this study. It is noteworthy that model 3 displayed a range of variation 2 times that of all other models. This may imply that the presences of a mixed failure mode may be the source of increased variability of results. From the results of the testing and fracture patterns on the implants, it appears that the implant with a curved edge is creating contact delamination failure with the through-growth and that the implant with a sharp edge is creating a tensile fracture. **Image 38 (a)** is the sharp through-growth block after testing. In the image, one can see that the sharp implant impinged into the block material and dug up some of the underlying foam beneath the through-growth. **Image 38 (b)** is the curved through-growth block after testing. In the curved blocks, none of the underlying foam block was dislodged. The curved implant created more of a crushing fracture where the foam block was crushed and pushed upwards. In the image below one can see that the surface area of the through-growth ring for the curved block was increased. This occurred because the crushed through-growth was pushed into the block as the implant continued to rise, causing an increase in the surface area of the through-growth ring. This is all representative of contact delamination. It is very different than how the sharp implant acted. The sharp implant created a cleaner fracture, where the through-growth fractures as the implant was extracted and then subsequently the fractured through-growth fell from the block.

(a)

(b)
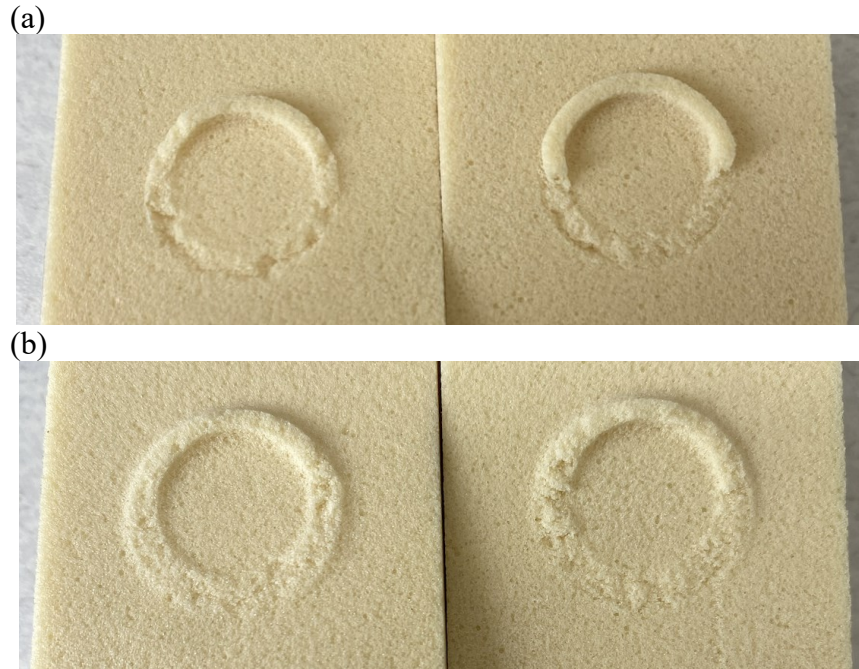
Image 38 Inside view of post testing (a) sharp through-growth foam blocks and (b) curved through-growth foam blocks

Microscope images of the through-growth after testing provide more detailed images of the fracture. In **Image 39 (a) and (b)** are the fractured edges of the remaining through-growth after testing. The sharp implant created a sharper or more crisp fracture where the through-growth is being cut off. This is more representative of a tensile fracture.

(a)   (b)

Image 39 Microscope images of sharp through-growth fracture

There was also a significant increase in the values of the implant with the curved edge with and without through-growth. The extraction force with through-growth and a curved edge was approximately 3 times greater than that without through-growth. From this difference and the manner that the curved implant fractured the foam blocks, one can infer that the curved implant would behave differently at different times post-operatively. The curved edge of the implant slides out fair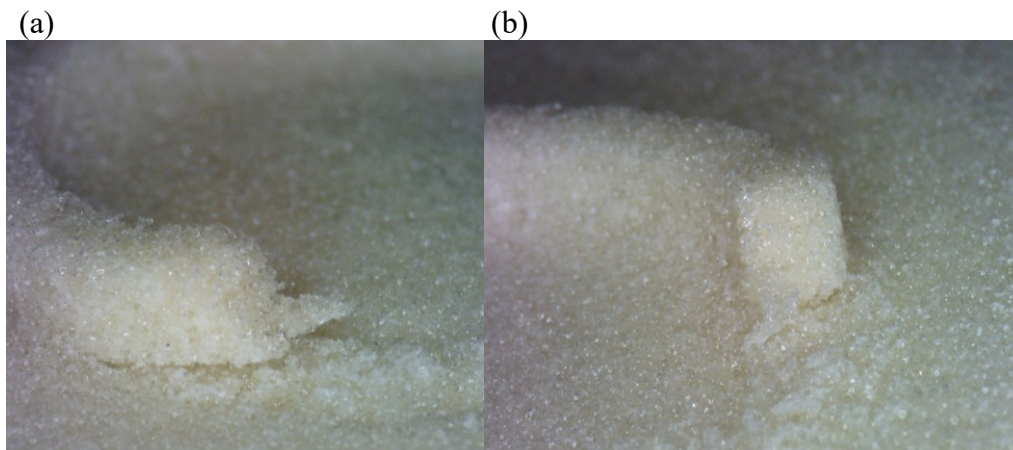ly easily at 0 weeks and no through-growth. You would expect at the beginning of growth, for the curved edge to be able to climb a lesser amount of through-growth due to the shape and the crushing mechanism that occurred. For example at 3 weeks with about 0.5 mm of through-growth, the implant may still be able to slide over the through-growth and extract without fracture. From the current data, one cannot conclude how the curved implant would act at these specific times, but it is clear that the implant would behave differently throughout the 8-week time period. It can be speculated that the implant's behavior may follow the patterns of an S curve and that the maximum load would continue to be low until the through-growth became a height that the implant could not climb past. The sharp implant would not follow a similar pattern, as the sharp edge catches onto the bone.

It is also important to note that the values for maximum load with through-growth are significantly higher than without through-growth. 112 kg for the curved edge with through-growth compared to 35.6 kg without through-growth and 103.67 kg for the sharp edge with through-growth compared to 91 without through-growth. The difference between sharp edge with and without through-growth is far less severe, which could imply that the sharp edge implant is more stable throughout the healing period compared to the curved edge implant and that the sharp edge is less reliant on through-growth for stability.

5.2 Simulation Testing

Abaqus FEA was used to perform the simulation testing to verify the experimental tests that were completed. The same four assemblies were tested on Abaqus for maximum load values. The relationships between sharp and curved edge implants and no through-growth versus through-growth implants were fairly similar to the experimental testing. Let's consider the simulation testing for a 0.2 coefficient of friction. The implant with a sharp edge and no through-growth had a maximum load of 295 N, whereas the implant with a curved edge and no through-growth only had a maximum load of 16 N. The implant with a sharp edge and through-growth had a maximum load of 410 N and the implant with a curved edge and through-growth had a maximum load of 92. Throughout all of the trials, the implants with curved edges had significantly lower maximum load values. This implies that implants with sharp edges would be more stable overall in a surgical site than an implant with a curved edge. The sharp edge allows the implant to catch onto the foam blocks. The implants with through-growth also had significantly higher values than their corresponding implant types without through-growth. This shows that there is more stability with the addition of through-growth. This allows us to predict that the most stable surgical implant would have a window with a sharp edge and be at least a few weeks after the surgery takes place.

There is a large difference between the values for the implants with the sharp edge versus the implants with the curved edge. The implants with a sharp edge always have at least 4 times the maximum load values compared to the implants with a curved edge. This could suggest that the fracture mechanisms are different. From the patterns seen with the data, it is predicted that the sharp edge with through-growth will have the highest maximum load, however, this extensive difference in values is predicted to be an error in the simulation. It appears that due to the failure mechanisms that should occur for the curved edge implant, Abaqus is unable to model

the extraction of the implant and created failure early. This will be discussed further in section **5.4.**

Abaqus analysis was also performed to understand the effect of changing friction between the implant and bone. Increasing friction had a significant effect on the stability of each of the implants except for the curved implant with through-growth. The implant with a sharp edge and no through-growth had a maximum load value of 295 N for the 0.2 coefficient of friction but increased to 1560 N for the 0.8 coefficient of friction. The implant with the curved edge and no through-growth had a maximum load value of 16 N with a 0.2 coefficient of friction but increased to 90 N with a 0.8 coefficient of friction. This indicates that friction plays a large role in the stability of an implant, directly post-operatively when there is no through-growth. The implant with the sharp edge and through-growth had a 410 N maximum load with 0.2 friction coefficient, and a 1520 N maximum load for a 0.8 friction coefficient. Friction is playing a large role in the stability of this implant. In contrast, the implant with a curved edge and through-growth has maximum values that stay within 4 N of each other. The maximum load value for 0.2 coefficient of friction is 92 N whereas the maximum load value for 0.8 coefficient of friction is 91 N. This again touches on the idea of an error in the simulation. The drastic increase in friction should have an effect on the maximum load. This will be explained further in section **5.4.**

These increases in maximum load from increasing friction suggest that the most stable surgical implant would have a rough surface at the interfaces between the bone and the implant. Initial stability is necessary for the success of this procedure. Initial stability is achieved when the forces required to remove the implant are equal to or less than the physiological forces that the implant bears postoperatively. Therefore, a rough surface will increase the coefficient of friction of the interaction between the tibia and the implant. This increased coefficient of friction

should lead to better surgical outcomes, as is supported by the data recorded. This supports the use of a porous trabecular metal coating being applied to the implant. Porous coatings encourage bone ingrowth which is necessary for long-term success and also increase surface roughness and friction.

5.3 Comparing Experimental and Simulation Results

The experimental testing and simulation testing results followed some similar patterns. In both the experimental and simulation testing the maximum load values were significantly higher for the models with through-growth. For the purpose of comparison, I will use the load values for the physical models in Newtons. The average maximum load for the physical sharp implant without through-growth is 892.4 N and 1016.6 N with through-growth. The average maximum load for the physical curved implant without through-growth is 349.1 N and 1098.3 N with through-growth. For both physical models, the maximum load increased greatly with through-growth. This also occurred with the simulation models. Using a 0.4 value for the coefficient of friction: the sharp model had a maximum load of 795.0 N without through-growth and a maximum load of 902.0 N with through-growth. Coefficient of friction was not measured for the physical models, however, through comparison it seems that the physical models had a coefficient of friction value similar to 0.4. The curved model had a maximum load value of 40.0 N without through-growth and an 88.0 N value with through-growth. This significant increase in values supports the idea that through-growth increases stability in all implants. There was only one instance (0.8 Coefficient of Friction) where there wasn't a dramatic increase in values with and without through-growth. This may be due to the fact that the simulation type used in Abaqus is unable to model the type of failure that occurred.

Both the experimental and simulation models also show a relationship between the maximum force and radius of curvature of the edge of the window on the implant. The sharp radius on average had higher maximum values than the curved radius. In the simulation testing, these values were always at least 4 times the value of the curved implant. For the experimental testing, the sharp implant had a significantly higher maximum load than the curved implant for the models without through-growth. However, for the models with through-growth, their maximum values were close together. The sharp radius had a maximum value of 1016.6 N and the curved had a value of 1098.3 N. The sharp radius had a range of values of 225.6 N and the curved radius had a range of value of 274.7 N. This large range of values makes sense considering that different amounts of the bone through-growth fractured in each trial. It is also expected because of the wide range in width difference for each of the trials, which impacted the compression acting on the assembly. For the trials with through-growth, it appeared that much of the force required to extract the implant came from the force required to fracture the through-growth.

Calculations were performed to find which coefficient of friction was most similar to the experimental testing data collected. Sum of squares calculations were used to find the difference between the experimental testing data to the values from each coefficient of friction. From these calculations, it seems that the 0.4 value of the coefficient of friction was most like the experimental testing values found.

The results of both the experimental and simulation testing suggest that the sharp radius is creating a tensile fracture through the through-growth and the curved radius is creating a contact delaminating failure through the through-growth. The experimental testing suggests this

through the way foam blocks are fractured and the simulation testing supports this by the different values between the curved versus sharp implants.

5.4 Critique of Methods & Future Work

An error in simulation testing was realized after analyzing the data and comparing it to the experimental results. Static analysis was used for the Abaqus simulation to show the maximum load allowed before failure. However, for the implant with the curved edge, "damaged plasticity" occurred which cannot be properly modeled in this static analysis. A Johnson-Cook Damage model would best represent the type of failure that occurred with the curved implant model. Johnson-Cook plasticity model is used for transient dynamic simulations and is a type of Mises plasticity model. This material model is able to represent the tearing, peeling, and compaction that occurs with the curved implant. In order to create this simulation, one would need to perform numerous material tests to find the specific material properties for closed-cell 20 pcf foam. These properties include temperature factor, strain rate fracture, and exponential factor. These properties are not available in the literature. Once these properties are found and the model is built, an accurate representation of the failure caused by the curved implant will be seen.

The experimental testing only included 3 trials per model. Within some of these trials, there were large ranges of maximum loads. Additional trials for each model would provide a more comprehensive understanding of the failure mechanisms.

The method for controlling compression for the experimental testing did not provide a compression value to analyze. Although an attempt was made to maintain a constant compression by measuring the width variation of the testing assembly, it was not feasible to ensure a consistent change in width for each trial. Increased compression results in increased

friction. As is evident from the simulation testing results, friction plays a large role in the maximum load values. The original plan for testing included a load cell within the foam blocks to provide a value for compression, this load cell had to be removed when the issue of keeping the foam blocks within the clamp came up during preliminary trials. Additionally, a plan to apply strain gages to the clamp was attempted. However, it was discovered that the clamp was too thick, and the strain gages were not sensitive enough to compression. Future studies should include higher sensitivity strain gages and a smaller clamp so compression values can be recorded and kept constant.

The material for the foam blocks used in experimental testing was purchased from Sawbones. The blocks were then fabricated at Scale Workspaces in New Orleans. While designing this testing procedure, the foam blocks were assumed to made of isotropic and homogenous material. However, it is unknown whether the through-growth areas behave isotropically. During fabrication, small fractures could have occurred in these precise areas that could affect their mechanical strength. This would affect the maximum load values and may account for the large ranges in some of the trials.

While going through the process of designing and fabricating the curved edge foam blocks, issues arose around the foam blocks fitting with the implant. The radius of the through-growth on the foam blocks had to be decreased by 0.3 mm. This caused there to be a small space between the through-growth and the implant window edge. This space may have also led to some variation for the implant with the curved edge and through-growth. An attempt was made to minimalize this variation by adding a small upward displacement during the simulation before the extraction force was applied.

For both experimental and simulation testing only the amount of force required for initial fracture and movement was recorded. Future studies should observe the complete extraction force for removing the implant from the testing assembly. For experimental testing, this could be done by increasing the width of the foam block assembly and the addition of clamps to hold the foam blocks in place after the implant is moved. The current method only holds the foam blocks while the implant is in place. Once the implant is extracted, the foam blocks fall. If the blocks were screwed into the side clamps or held in place by some other method, then they could stay in position for the duration of the testing.

For simulation testing, this can be done using a more advanced model on Abaqus FEA software. Models using smooth particle hydrodynamics and element deletion could be used to help capture a full picture of the extraction. Fracture analysis techniques would be helpful to see the full extraction. Since the curved-edge implant needs to be modeled using a Johnson-Cook plasticity model, this should be used in all four of the models to have the most accurate representation of maximum load. The current techniques do not show a clear picture of whether the foam blocks are being fully fractured and are not the most accurate techniques for this type of failure.

For both experimental and simulation testing only 0 mm of bone growth and 2 mm of bone through-growth were tested. This allowed visualization of stability directly after surgery and after about 8 weeks of healing. Future studies should include a wider variety of depths of bone through-growth. 0 mm, 0.5 mm, 1.0 mm, 1.5 mm, and 2 mm of bone growth would provide a comprehensive picture of how the different implants act throughout the 8-week healing period.

An implant with a sharp radius of curvature and an implant with a 2 mm radius of curvature were tested in both the experimental and simulation testing. This allowed us to

visualize how a completely sharp radius compared to a curved radius, however, a study with a larger number of radii would provide a more optimized value of the best implant for stability within the surgical site.

Convergence testing in Abaqus FEA software was not completed for this study. It was deemed unnecessary for the scope of this study because the purpose was to gain a qualitative understanding of the relationships. The assembly was seeded to a particle size of 0.2 mm and meshed using a tetrahedral shape. A convergence test should be completed in future studies. A smaller particle size provides more accurate data for this model. A smaller mesh should be used in future studies to provide the most accurate data. A hexahedral mesh should also be used for future studies, as hexahedral meshes can be subdivided anisotropically without the mesh quality problems that occur with a tetrahedral shape. Hexahedral meshes generally yield more accurate solution values.

5.5 Conclusion

This study focused on the effects of windows in an orthopedic interpositional implant and how to optimize these windows as a design feature. It found that windows can increase mechanical stability through the inclusion of through-growth into the windows. A sharper radius of curvature on the edges of windows provides increased initial stability for implants. It also found that 2 mm of through-growth is effective in increasing long-term mechanical stability. The results suggest that clinically the compression across this implant would provide the stability needed for success. Through-growth is not a concept that is studied frequently and the results of this pilot study support that future work on this concept would be beneficial to optimize and guide the use of windows not only for the MTOWI HTO implants but also for other orthopedic implants that incorporate them in their design. Additional studies with additional radii of

curvature and depths of through-growth would be beneficial. Orthopedic surgeons should choose interpositional implants that have windows with sharper edges to increase the initial and long-term stability of the implant in situ.
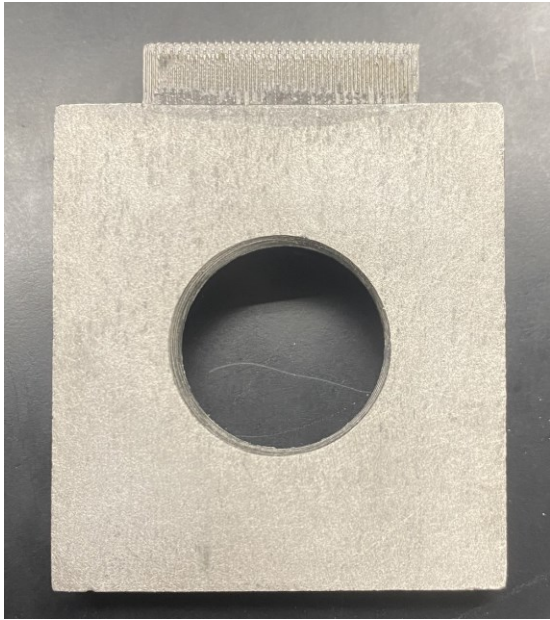
APPENDIX A: PHOTOS OF STAINLESS-STEEL IMPLANTS
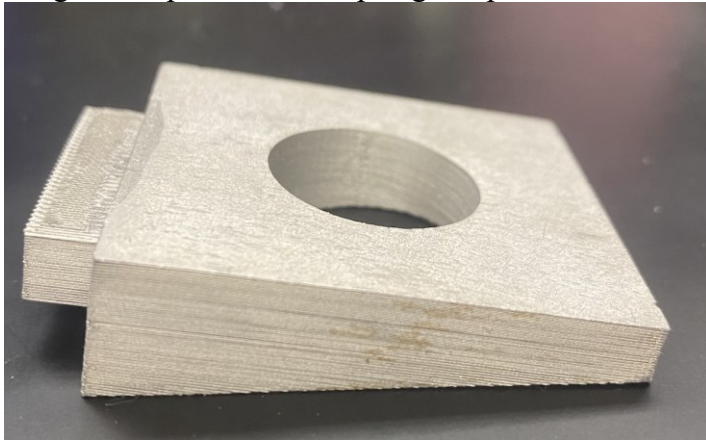

Image 38 Implant with sharp edge: superior view

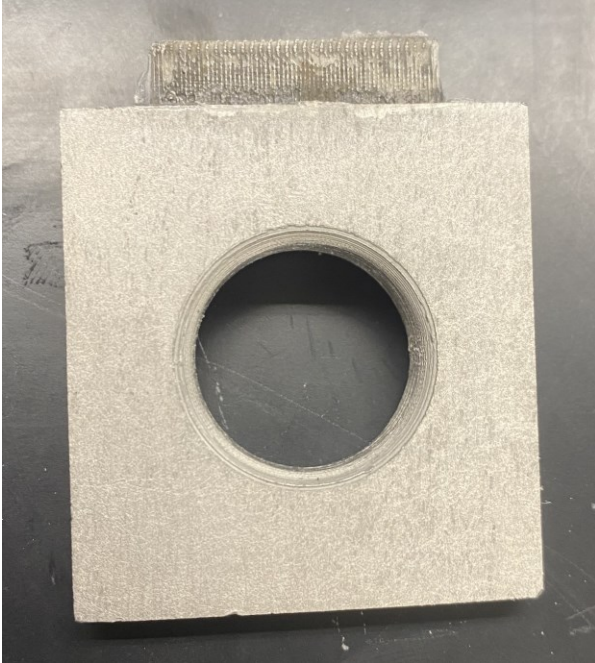Image 39 Implant with sharp edge: medial view

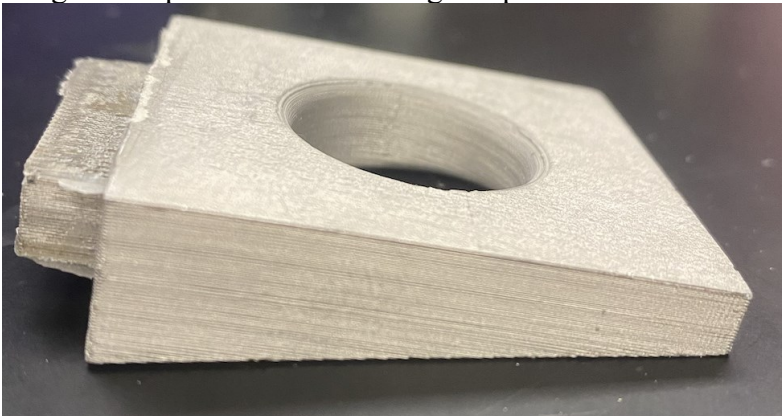Image 40 Implant with curved edge: superior view

Image 41 Implant with sharp edge: medial view

APPENDIX B: PHOTOS OF FOAM BLOCKS

Curved edge no through-growth

Image 42 Trial 1

Image 43 Trial 2

Image 44 Trial 3

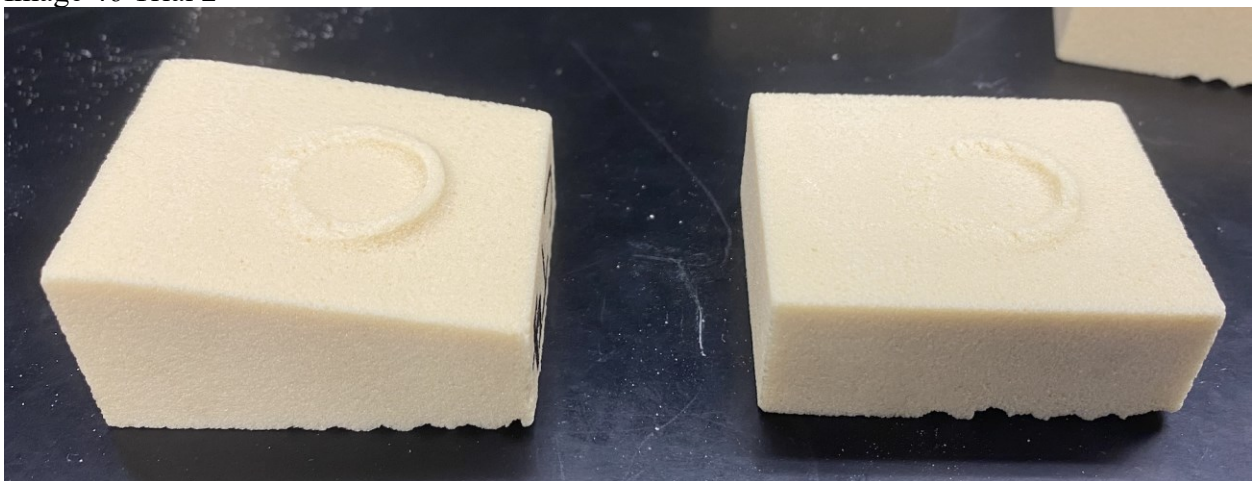Curved edge with through-growth

Image 45 Trial 1

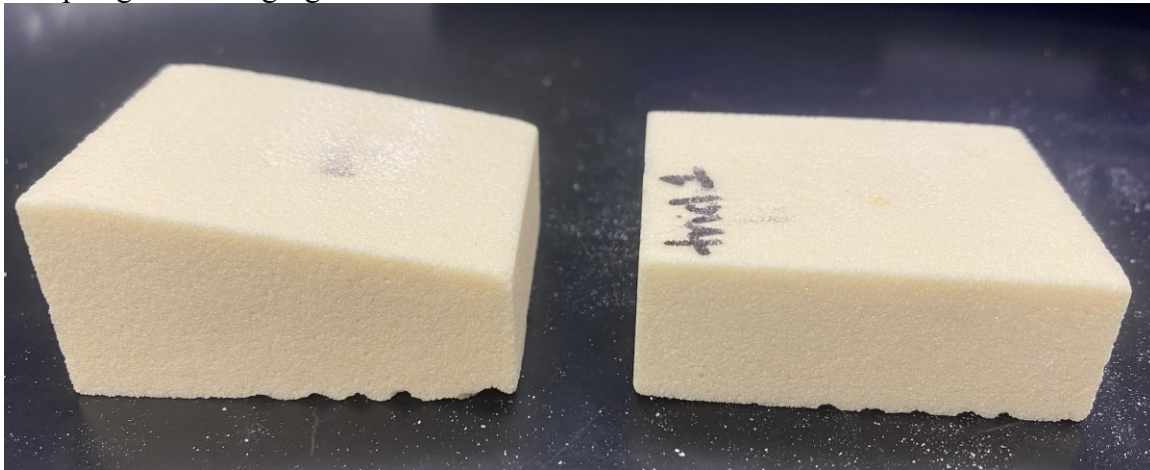Image 46 Trial 2

Image 47 Trial 3

Sharp edge no through-growth

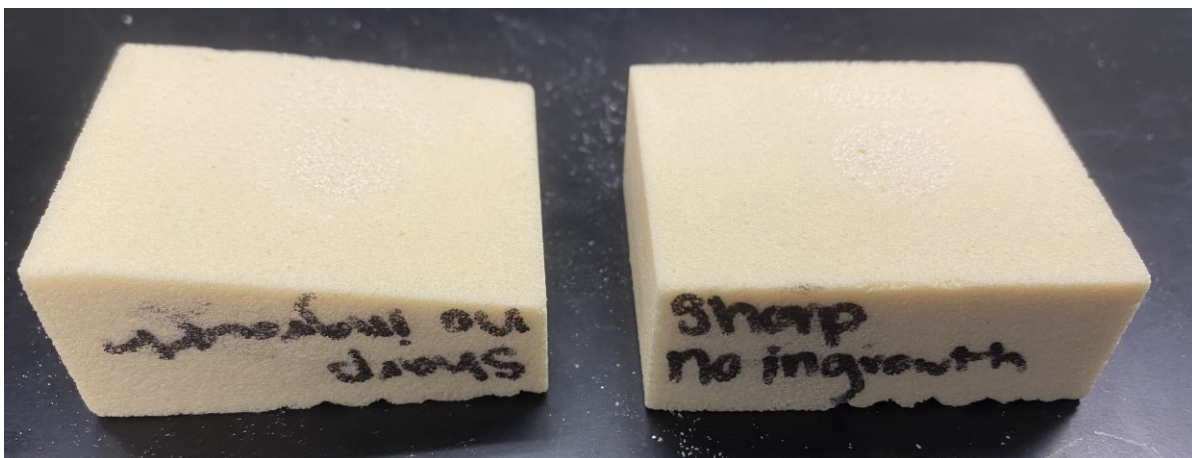Image 48 Sharp edge no through-growth trial 1

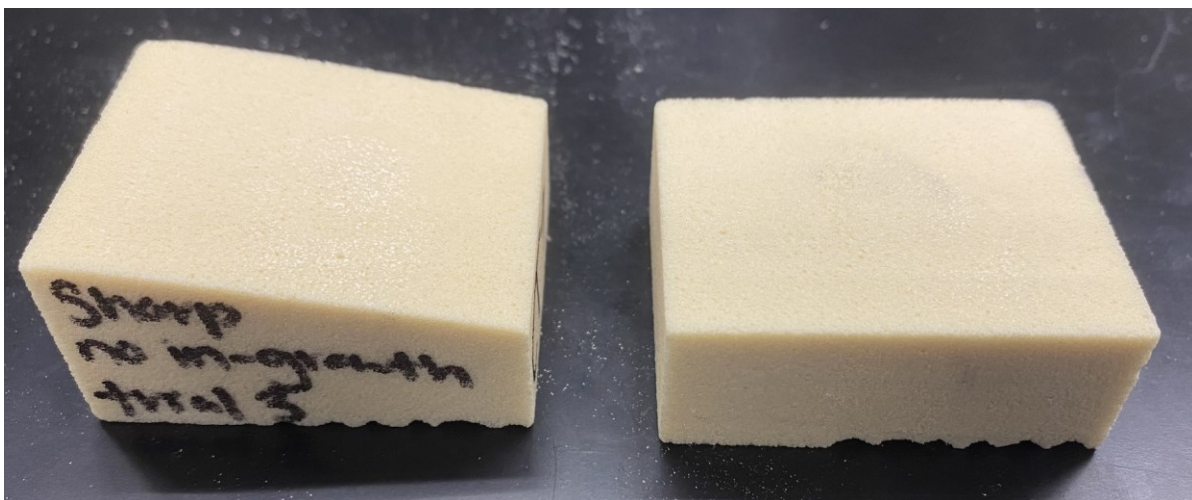Image 49 Sharp edge no through-growth trial 2

Image 50 Sharp edge no through-growth trial 2
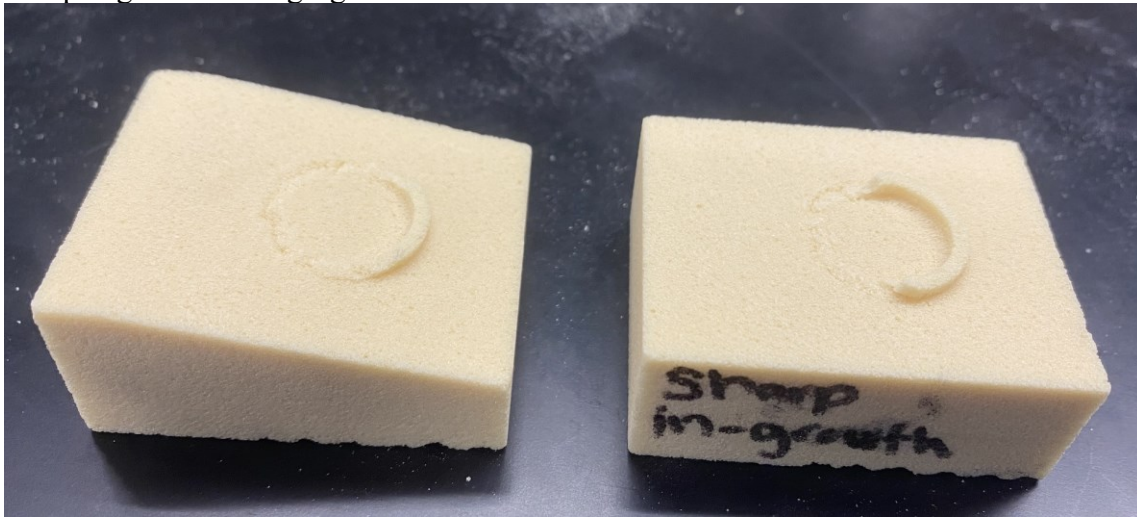
Sharp edge with through-growth

Image 51 Trial 1

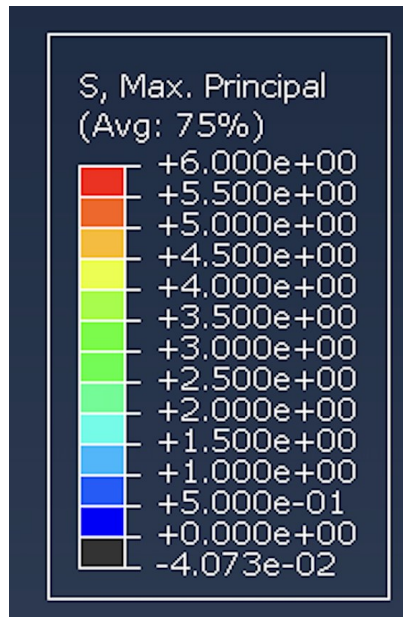Image 52 Trial 2

Image 53 Trial 3

APPENDIX C: PHOTOS OF SIMULATION RESULTS (MAX PRINCIPAL STRESSES)

Image 54 Color Map of max principal stress in MPa.

Image 55 Computation results of max principal stress for 0.2 value of coefficient of friction in isometric view comparing: (a) curved edge without through-growth from maximum load of , (b) sharp edge without through-growth, (c) curved edge with through-growth, (d) sharp edge with through-growth.
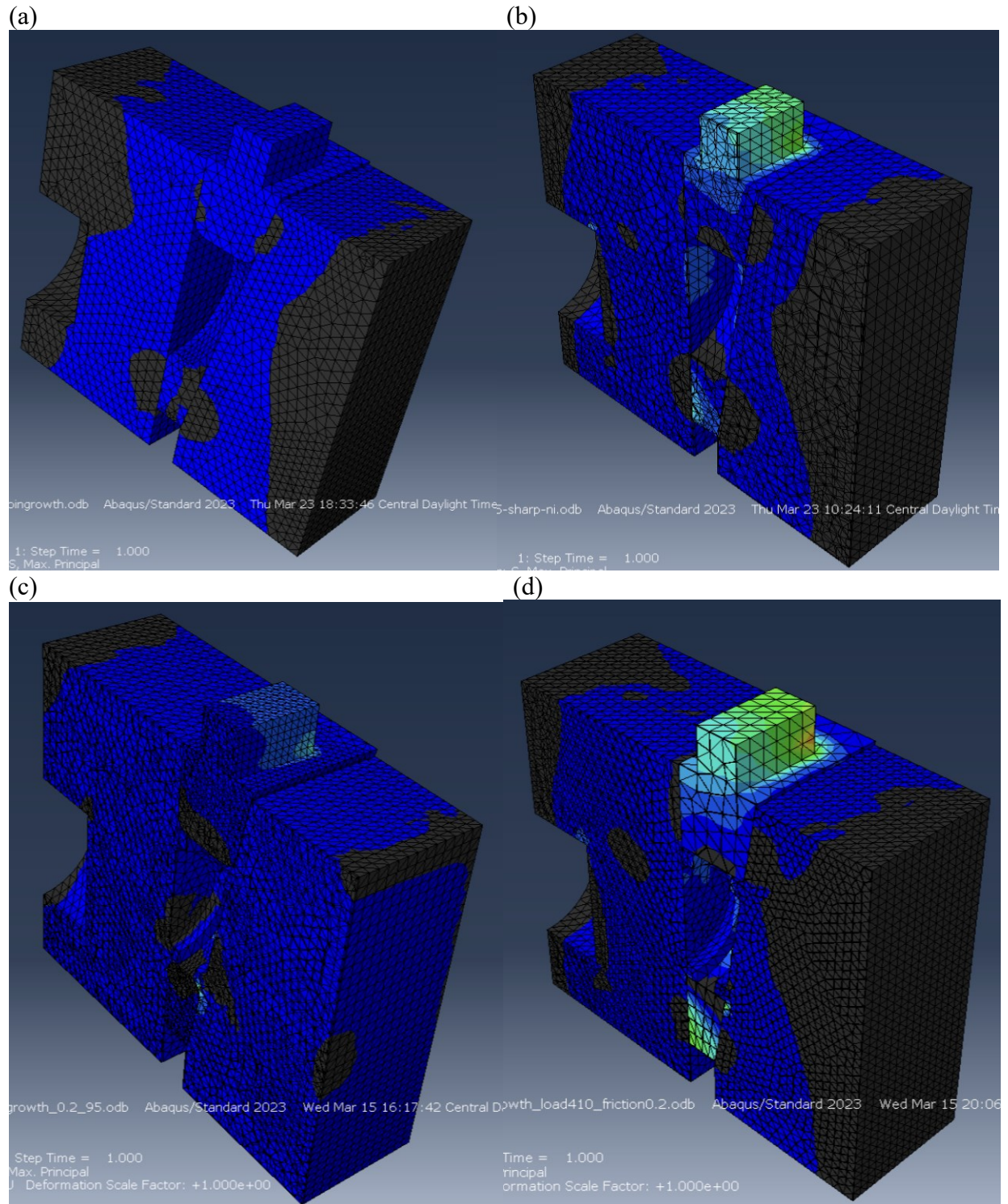
Image 56 Computation results of max principal stress for 0.4 value of coefficient of friction in isometric view comparing: (a) curved edge without through-growth from maximum load of , (b) sharp edge without through-growth, (c) curved edge with through-growth, (d) sharp edge with through-growth.

(a)

(b)

(c)

(d)

Image 57 Computation results of max principal stress for 0.8 value of coefficient of friction in isometric view comparing: (a) curved edge without through-growth from maximum load of , (b) sharp edge without through-growth, (c) curved edge with through-growth, (d) sharp edge with through-growth.
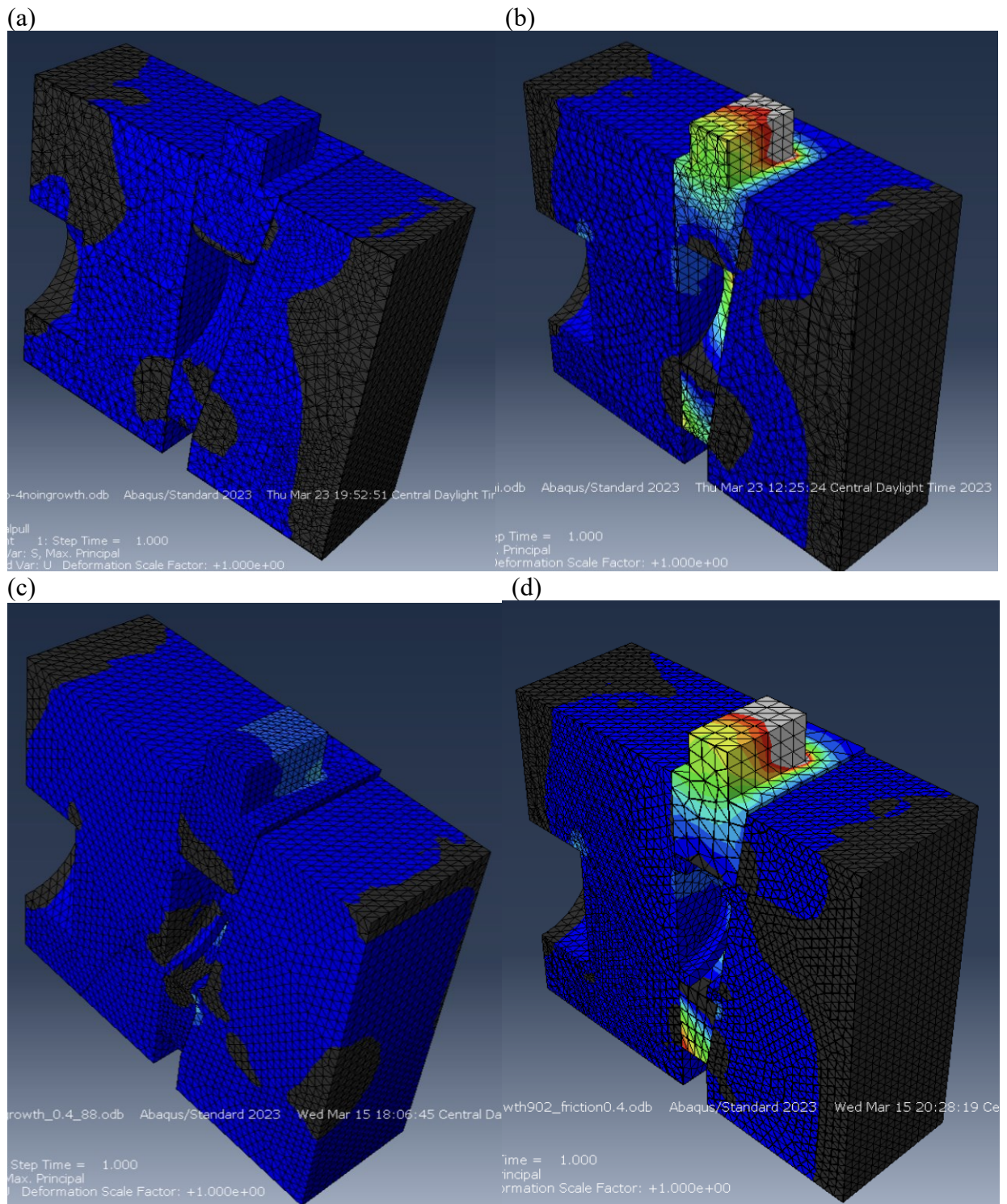
APPENDIX D: PHOTOS OF SIMULATION RESULTS (MIN PRINCIPAL STRESSES)

Image 58 Color Map of min principal stress in MPa.

Image 59 Computation results of minimum principal stress for 0.2 value of coefficient of friction in isometric view comparing: (a) curved edge without through-growth from maximum load of , (b) sharp edge without through-growth, (c) curved edge with through-growth, (d) sharp edge with through-growth.
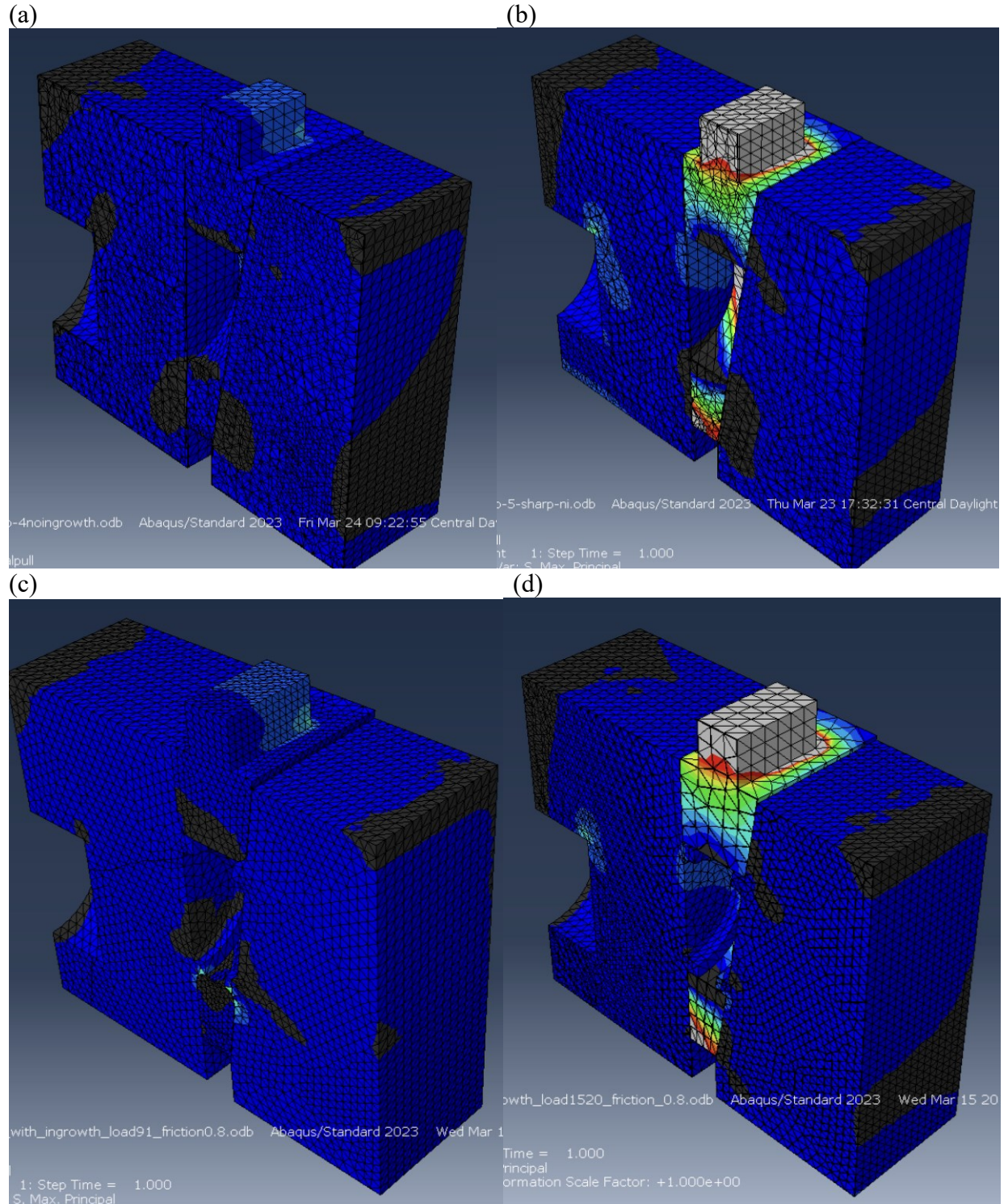
(a)

(b)

(c)

(d)

Image 60 Computation results of minimum principal stress for 0.4 value of coefficient of friction in isometric view comparing: (a) curved edge without through-growth from maximum load of , (b) sharp edge without through-growth, (c) curved edge with through-growth, (d) sharp edge with through-growth.
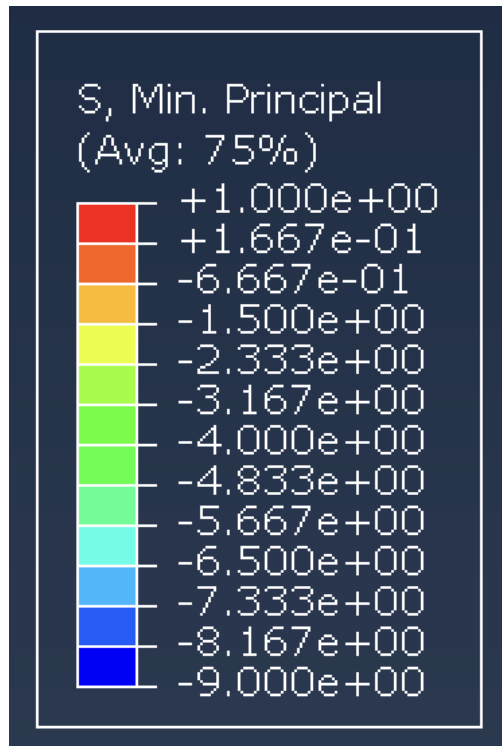
(a)

(b)

(c)

(d)

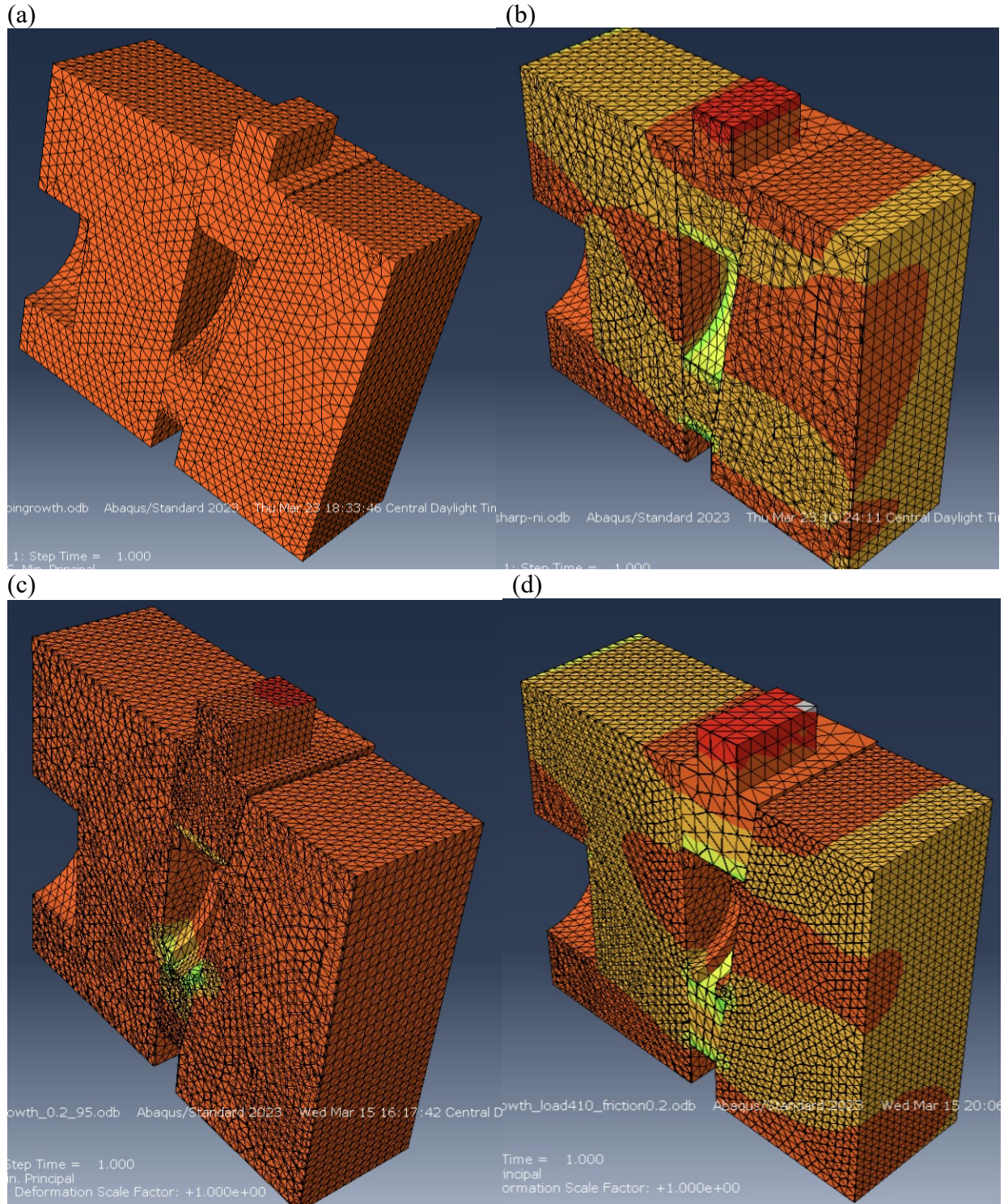
Image 61 Computation results of max principal stress for 0.8 value of coefficient of friction in isometric view comparing: (a) curved edge without through-growth from maximum load of , (b) sharp edge without through-growth, (c) curved edge with through-growth, (d) sharp edge with through-growth.
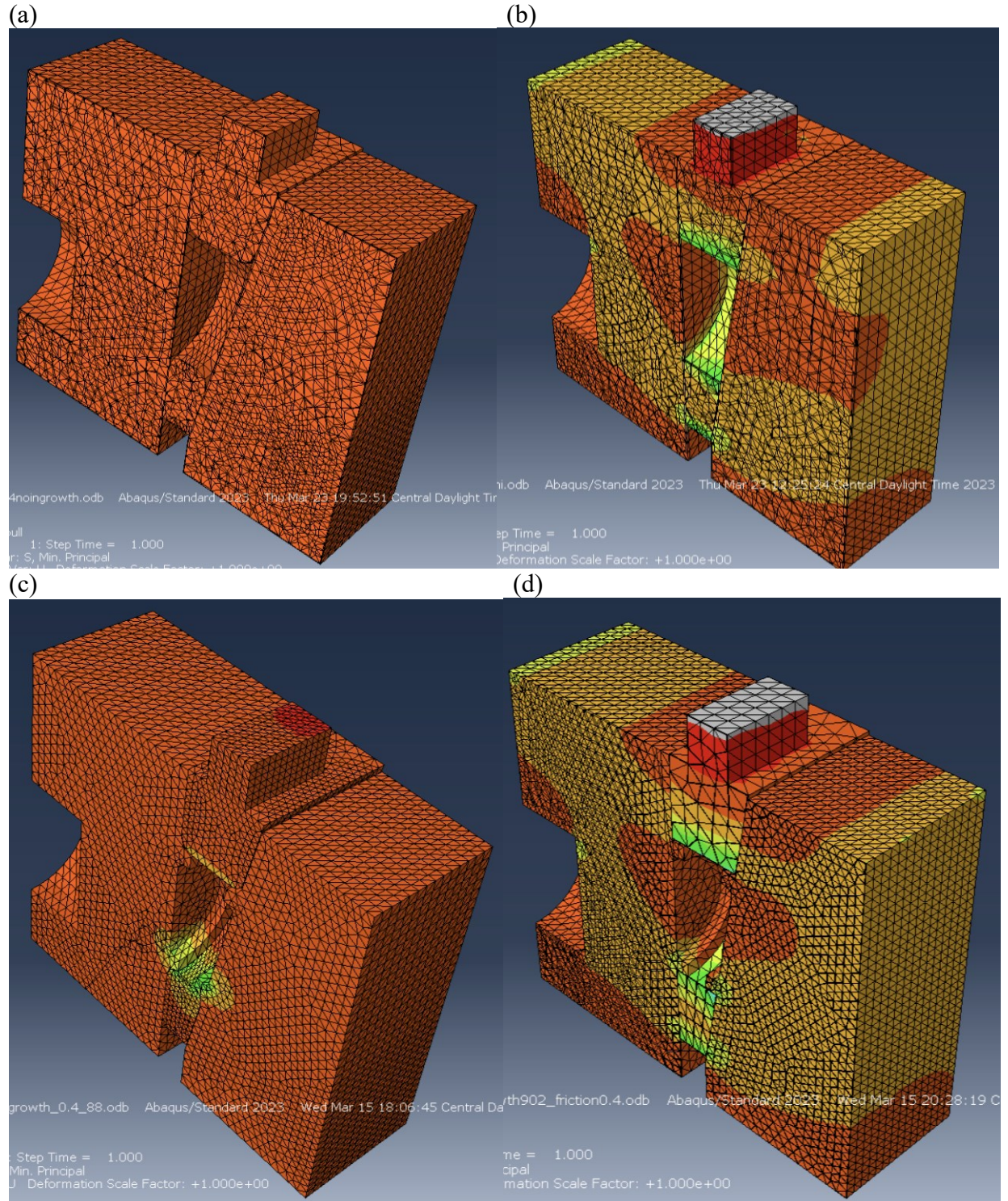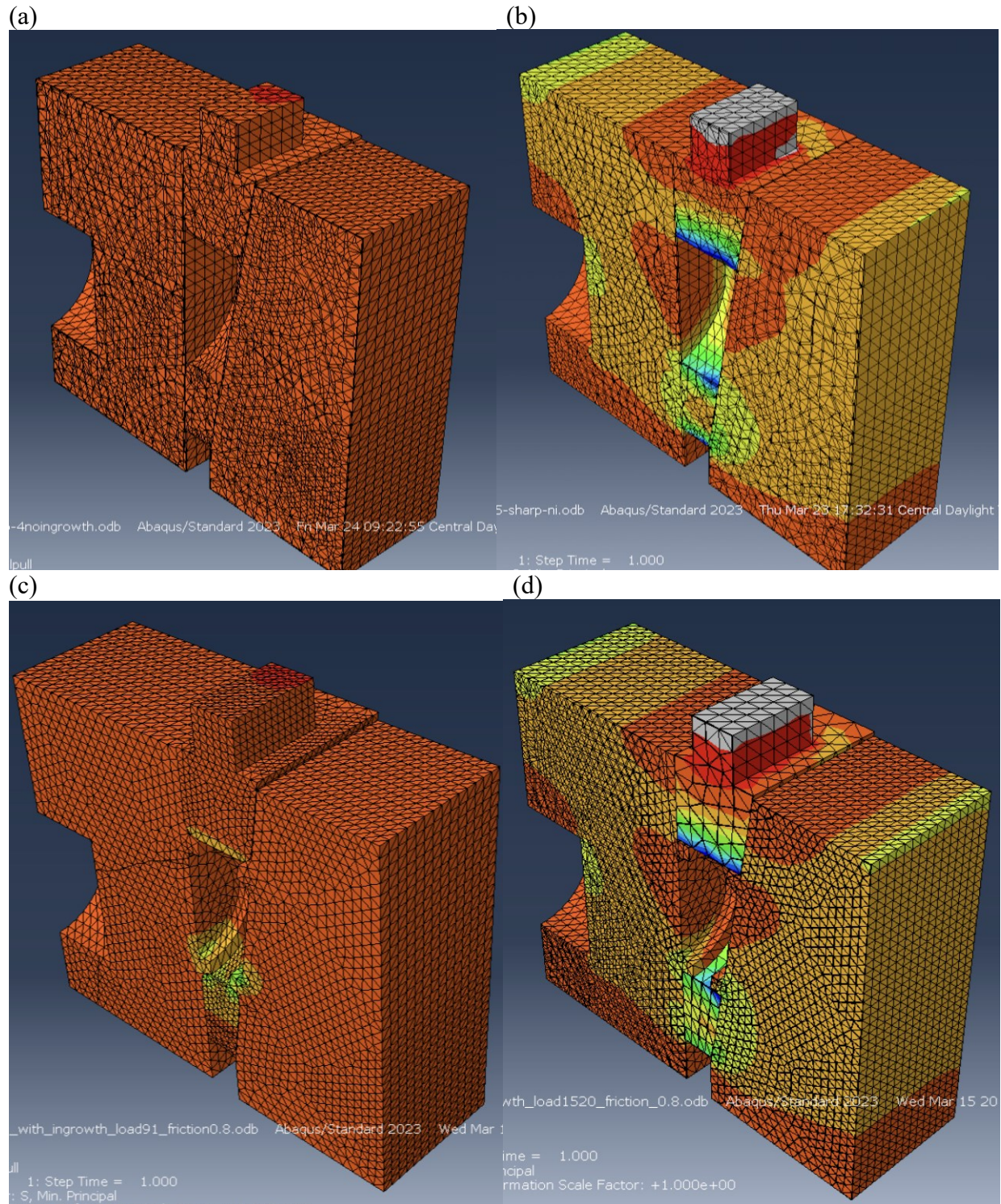
LIST OF REFERENCES

4WEB Medical. (n.d.). *Osteotomy Truss System: 4WEB Medical Surgical Technique*. Frisco, Texas.

4WEB Medical. (n.d.). *Analysis of a Modified Evans Osteotomy using 4WEB Medicals Osteotomy Truss System*. Frisco, Texas.

Betts, J. G., Desaix, P., Johnson, E., Johnson, J. E., Korol, O., Kruse, D., Poe, B., Wise, J., Womble, M. D., & Young, K. A. (2022). Bone Tissue and the Skeletal System: Bone Structure. In *Anatomy and Physiology*. essay, OpenStax, Rice University.

Bowker, J. H. (1992). Surgical, Prosthetic, and Rehabilitation Principles. In *Atlas of Limb Prosthetics* (2nd ed.). essay, American Academy of Orthopedic Surgeons.

Boyce, L., Prasad, A., Barrett, M., Dawson-Bowling, S., Millington, S., Hanna, S. A., & Achan, P. (2019). The outcomes of total knee arthroplasty in morbidly obese patients: A systematic review of the literature. *Archives of Orthopaedic and Trauma Surgery*, *139*(4), 553–560. https://doi.org/10.1007/s00402-019-03127-5

Budynas, R. G., Nisbett, J. K., & Shigley, J. E. (2008). Failures Resulting from Static Loading. In *Shigley's Mechanical Engineering Design* (8th ed., pp. 211–231). essay, McGraw-Hill.

Campi, S., Papalia, G. F., Esposito, C., Albo, E., Cannata, F., Zampogna, B., Papalia, R., & Denaro, V. (2021). Unicompartmental knee replacement in obese patients: A systematic review and meta-analysis. *Journal of Clinical Medicine*, *10*(16). https://doi.org/10.3390/jcm10163594

Chen, D., Shen, J., Zhao, W., Wang, T., Han, L., Hamilton, J. L., & Im, H.-J. (2017). Osteoarthritis: Toward a comprehensive understanding of pathological mechanism. *Bone Research*, *5*(1). https://doi.org/10.1038/boneres.2016.44

Cross, M. J., & Spycher, J. (2008). Cementless fixation techniques in joint replacement. *Joint Replacement Technology*, 190–211. https://doi.org/10.1533/9781845694807.2.190

Cui, A., Li, H., Wang, D., Zhong, J., Chen, Y., & Lu, H. (2020). Global, regional prevalence, incidence and risk factors of knee osteoarthritis in population-based studies. *EClinicalMedicine*, *29-30*. https://doi.org/10.1016/j.eclinm.2020.100587

Grujicic, R. (2022, December 5). *Gait cycle*. Kenhub. Retrieved April 21, 2023, from https://www.kenhub.com/en/library/anatomy/gait-cycle

Guo, Y., Zhang, X., & Chen, W. (2009). Three-Dimensional Finite Element Simulation of Total Knee Joint in Gait Cycle. *Acta Mechanica Solida Sinica*, *22*(4), 347–351. https://doi.org/10.1016/s0894-9166(09)60283-4

Gupton, M., Imonugo, O., & Terreberry, R. R. (2022, November 15). *Anatomy, Bony Pelvis and Lower Limb, Knee*. StatPearls [Internet]. Retrieved from https://www.ncbi.nlm.nih.gov/books/NBK500017/

Heidari, B. (2011). Knee osteoarthritis prevalence, risk factors, pathogenesis and features: Part I. *Caspian Journal of Internal Medicine*, *2*(2).

Herbst, M., Ahrend, M.-D., Grünwald, L., Fischer, C., Schröter, S., & Ihle, C. (2021). Overweight patients benefit from high tibial osteotomy to the same extent as patients with normal weights but show inferior mid-term results. *Knee Surgery, Sports Traumatology, Arthroscopy*, *30*(3), 907–917. https://doi.org/10.1007/s00167-021-06457-3

Hunter, D. J., Sharma, L., & Skaife, T. (2009). Alignment and osteoarthritis of the knee. *Journal of Bone and Joint Surgery*, *91*(Supplement_1), 85–89. https://doi.org/10.2106/jbjs.h.01409

Jain, S., Eltorai, A. E., Ruttiman, R., & Daniels, A. H. (2016). Advances in spinal interbody cages. *Orthopaedic Surgery*, *8*(3), 278–284. https://doi.org/10.1111/os.12264

Khakha, R. S., Bin Abd Razak, H. R., Kley, K., van Heerwaarden, R., & Wilson, A. J. (2021). Role of high tibial osteotomy in medial compartment osteoarthritis of the knee: Indications, surgical technique and outcomes. *Journal of Clinical Orthopaedics and Trauma*, *23*, 101618. https://doi.org/10.1016/j.jcot.2021.101618

King, L. K., & Anandacoomarasamy, A. (2013). Obesity & osteoarthritis. *Indian Journal of Medical Research*, *138*(2), 185–193.

Lagier, R. (2006). Bone Eburnation in rheumatic diseases: A guiding trace in today's radiological diagnosis and in paleopathology. *Clinical Rheumatology*, *25*(2), 127–131. https://doi.org/10.1007/s10067-004-1055-8

Lespasio, M. J., Piuzzi, N. S., Husni, M. E., Muschler, G. F., Guarino, A. J., & Mont, M. A. (2017). Knee osteoarthritis: A Primer. *The Permanente Journal*, *21*(4). https://doi.org/10.7812/tpp/16-183

Liu, X., Chen, Z., Gao, Y., zhang, J., & Jin, Z. (2019). High tibial osteotomy: Review of techniques and Biomechanics. *Journal of Healthcare Engineering*, *2019*, 1–12. https://doi.org/10.1155/2019/8363128

Loeser, R. F. (2010). Age-Related Changes in the Musculoskeletal System and the Development of Osteoarthritis. *Clinics in Geriatric Medicine*, *26*(3), 371–386. https://doi.org/10.1016/j.cger.2010.03.002

McCormack, D. J., Puttock, D., & Godsiff, S. P. (2021). Medial compartment osteoarthritis of the knee: A review of surgical options. *EFORT Open Reviews*, *6*(2), 113–117. https://doi.org/10.1302/2058-5241.6.200102

Michael, J. W.-P., Schlüter-Brust, K. U., & Eysel, P. (2010). The Epidemiology, Etiology, Diagnosis, and Treatment of Osteoarthritis of the Knee. *Deutsches Ärzteblatt International*. https://doi.org/10.3238/arztebl.2010.0152

Nahian, A., & Davis, D. D. (2022). Histology, Osteoprogenitor Cells. In *StatPearls [Internet]*. essay, StatPearls Publishing.

National Heart, Lung, and Blood Institute, & Pi-Sunyer, X., 00-4084The Practical Guide: Identification, Evaluation, and Treatment of Overweight and Obesity in Adults (2000). U.S. Department of Health and Human Services.

Pazzinatto, M. F., de Oliveira Silva, D., Faria, N. C., Simic, M., Ferreira, P. H., Azevedo, F. M., & Pappas, E. (2019). What are the Clinical Implications of Knee Crepitus to Individuals with Knee Osteoarthritis? an Observational Study with Data from the Osteoarthritis Initiative. *Brazilian Journal of Physical Therapy*, *23*(6), 491–496. https://doi.org/10.1016/j.bjpt.2018.11.001

Pontius, U. R. (2020, January 16). Method and Apparatus for Orthopedic Implant.

Rönn, K., Reischl, N., Gautier, E., & Jacobi, M. (2011). Current surgical treatment of knee osteoarthritis. *Arthritis*, *2011*, 1–9. https://doi.org/10.1155/2011/454873

Sawbones USA. (2022). *Top Biomechanical Products & Materials Provider For Testing & Validation*. Sawbones. Retrieved April 25, 2023, from https://www.sawbones.com/biomechanical-product-info

Schiraldi, M., Bonzanini, G., Chirillo, D., & de Tullio, V. (2016). Mechanical and kinematic alignment in total knee arthroplasty. *Annals of Translational Medicine*, *4*(7), 130–130. https://doi.org/10.21037/atm.2016.03.31

Sheen, J. R., & Garla, V. V. (2022). Fracture Healing Overview. In *StatPearls [Internet]*. essay, StatPearls Publishing.

Sparr, A. (2022, December 7). *Properties of grade 5 titanium (TI6AL4V or TI 6-4)*. Parts Badger. Retrieved April 23, 2023, from https://parts-badger.com/properties-of-grade-5-titanium/

Spillane, D. M., Harris, C. S., Junker, M. C., Figel, A. E., Tallman, M. G., Kinney, S. R., Anderson, R. C., & Pontius, U. R. (2021). A multi-component implant for use in tibial osteotomy to correct varus deformity in the morbidly obese. *Biomedical Sciences Instrumentation*, *57*(4), 486–492. https://doi.org/10.34107/kszv7781.10486

Todinov, M. T. (2007). Locally initiated failure and risk reduction. *Risk-Based Reliability Analysis and Generic Principles for Risk Reduction*, 315–345. https://doi.org/10.1016/b978-008044728-5/50016-0

van Rossom, S., Smith, C. R., Thelen, D. G., Vanwanseele, B., Van Assche, D., & Jonkers, I. (2018). Knee Joint Loading in Healthy Adults during Functional Exercises: Implications for Rehabilitation Guidelines. *Journal of Orthopaedic & Sports Physical Therapy*, *48*(3), 162–173. https://doi.org/10.2519/jospt.2018.7459

Wang, S.-T., & Ni, G.-X. (2022). Depression in osteoarthritis: Current understanding. *Neuropsychiatric Disease and Treatment*, *Volume 18*, 375–389. https://doi.org/10.2147/ndt.s346183

Wei, C., Xie, W., Zhang, W., Tang, N., Su, Y., Jiang, B., Walschot, L. H., Xu, H., Li, Y., & Huang, T. (2022). New insight into the current study of high tibial osteotomy: A Bibliometric analysis. *Medicine*, *101*(37). https://doi.org/10.1097/md.0000000000030357

What is von mises stress in fea? SimScale. (2023, March 9). Retrieved April 26, 2023, from https://www.simscale.com/docs/simwiki/fea-finite-element-analysis/what-is-von-mises-stress/#:~:text=Von%20Mises%20stress%20is%20a,ductile%20materials%2C%20such%20as%20metals.

Zhang, Y., & Jordan, J. M. (2010). Epidemiology of Osteoarthritis. *Clinics in Geriatric Medicine*, *26*(3), 355–369. https://doi.org/10.1016/j.cger.2010.03.001

BIOGRAPHY

Tara Parker grew up in New Delhi, India where her love of biomedical sciences started. Tara received her M.S. in Biomedical Engineering in May of 2023 from Tulane University. She graduated with a B.S.E degree in May of 2022. She majored in Biomedical engineering with a minor in Economics. She developed her interests in medical device design and orthopedics throughout her time at Tulane University. Tara will continue to work for Dr. Uwe Pontius on his HTO implant design in the future.